POLITECNICO DI TORINO

Master's Degree in Mechatronic Engineering

Master's Degree Thesis

Wireless Charging and Power Management System for Biomedical Implantable Devices

Supervisors

Prof. Danilo Demarchi

Ph.D. Paolo Motto Ros

M.Sc. Fabiana Del Bono

Candidate

Andrea Dentis

JULY 2023

Abstract

Wireless Power Transfer (WPT) has recently been increasingly demanded in various engineering fields, from automotive to Active Implantable Medical Devices (AIMDs), due to the increased use of mobile devices, which, being battery-powered, require recharging. Replacement or wired charging may be impractical, expensive, risky, or even impossible for some devices. For these devices, WPT offers an alternative charging method that can overcome these issues. In the case of AIMDs, WPT allows to avoid battery replacement and thus the risk connected with surgical intervention. This thesis addresses the wireless charging and power management development of the Nanochannel Delivery System (nDS), a remotely controllable active implantable device for drug delivery. The device includes a reservoir containing the drug, refillable through transcutaneous injection, and a circuit that manages its operation. It will be helpful for chronic diseases such as rheumatoid arthritis or hypertension, which usually require continuous therapy. Thanks to a nanofluidic silicon membrane, whose release rate is electrically controllable by applying a voltage, nDS can provide personalized therapy for the patient. The doctor can remotely manage the drug release profile through Bluetooth Low Energy(BLE) communication. This work aims to develop Wireless Power Transfer and circuit suitable for safely recharging an implanted Li-Ion battery. To this end, the requirements to be considered are: optimal receiver and optimal receiver's coil in terms of size and efficiency, reliability of the charging process, high power transmission efficiency, low heat dissipation, and low sensitivity to any misalignments between receiver (RX) and transmitter (TX). The investigated RX, including LTC4124 and LTC4126, utilized near-field inductive coupling (NRIC) for wireless power transfer, while the LTC4125 was employed as the TX. Modifications on the LTC4125 were developed to test different coils, and custom boards for the receivers were designed. The system relies on closed-loop control where the microcontroller of the RX communicates with the transmitter to increase or decrease the power to be transferred to achieve maximum efficiency, according to an algorithm. In the final device, the loop is closed via BLE, which is already used to control the device. Through efficiency analysis, the tests aimed to find the optimal receiver coil in terms of size and efficiency. Different spatial configurations between coils have been tested to account for potential misalignment between the implanted device's RX and TX coil. The power delivered by the transmitter (P_t) and the power absorbed by the battery (P_b) are measured, and the efficiency is calculated. In addition, tests were carried out to investigate the complete battery recharge process and to analyze possible variations in efficiency and heat dissipation. These tests aimed to emulate the behavior of the implanted device; thus, tests with interposition of material, such

as saline solution or animal tissue, were included. The results demonstrated that the LTC4124 is a better receiver for this application and that the coil with 19 mm diameter has the best performance among all the tested coils, achieving 30% of efficiency at 6.5 mm distance between RX and TX coil. The design of the final board incorporated the LTC4124 and the utilization of a 19 mm coil. This combination ensured robustness against misalignments in future in-vivo tests, high efficiency, and minimal temperature increase.

Acknowledgements

I want to thank my supervisors, Danilo Demarchi, Paolo Motto Ros, and Fabiana Del Bono, for supporting and guiding me throughout this journey. I would also like to thank my family for always supporting and believing in me. Then I would like to thank my friends for always being by my side over the years. And finally, I would like to thank my Piri for being my Light.

Table of Contents

Acronyms

WPT Wireless Power Transfer

AIMD Active Implantable Medical Device

NRIC Near-Field Resonant Inductive Coupling

NCC Near-Field Capacitive Coupling

UTET Ultrasonic Transcutaneous Energy Transfer

nDS Nanochannel Delivery System

BLE Bluetooth Low Energy

MCU Microcontroller Uni

DAC Digital Analog Converter

ADC Analog Digital Converter

TX Transmitter

RX Receiver

SP Series Parallel

SS Series Series

PS Parallel Series

PP Parallel Parallel

AC Alternating Current

DC Direct Current

IC Integrated Circuit

UVCL Under Voltage Current Limiting

CC Constant Current

CV Constant Voltage

NTC Negative Temperature Coefficient

ITH Input current Threshold

ILIM Input current Limit

DTH Differential Tank Threshold

ASCI Application-Specific Integrated Circuit

CPU Central Processor Unite

List of Tables

List of Figures

Chapter 1

Introduction

Although Wireless Power Transfer (WPT) is a technology that has been known since the nineteenth century and proposed for the first time by Nikola Tesla [1], it has only recently been increasingly demanded in various engineering fields, from automotive to Active Implantable Medical Devices (AIMDs) [2]. WPT enables the transfer of electrical energy from a power source to a device wirelessly. The AIMDs require batteries to be powered, and the WPT system offers significant advantages to these devices, allowing battery recharging without a physical connection. This technology overcomes the problem of surgery for battery replacement or wired charging, increasing the safety of the AIMD. However, implementing the WPT system in biomedical applications is still challenging since it needs to consider parameters such as the size of the WPT system, biocompatibility, heat dissipation, and efficiency. Various WPT techniques have been adopted to accomplish this challenge, including Near-Field Resonant Inductive Coupling (NRIC) [3], Near-Field Capacitive Coupling (NCC) [4], and Ultrasonic Transcutaneous Energy Transfer (UTET) [5]. Among these WPT strategies, NRIC is considered the optimal WPT method for powering AIMDs as it meets their power requirements without damaging the surrounding tissue [2]. The objective of this thesis is the implementation of the WPT system and the power management of the Nanochannel Delivery System (nDS). nDS is a remotely controlled implantable device for drug delivery to manage the drug doses to patients who suffer from chronic pathologies [6]. This dissertation introduces the WPT system, nDS, and the objective of this research.
Chapter 2 presents the nDS description, the state of the art of the WPT systems, the nDS requirements to implement a WPT system, the description of the receiver LTC4124, the description of the receiver LTC4126, and studies a developed closed-loop WPT system
Chapter 3 presents the interventions made on the studied closed-loop WPT system.
Chapter 4 presents the tests and the results obtained with the modified WPT system. First, the comparison between LTC4124 and LTC4126 receivers, secondly

the characterizations of different receiver coils alongside recharge test and lastly, evaluation and optimization of the control loop algorithm.
Chapter 5 analyzes the design of the receiver board for nDS, with the introduction of the Recharge Status Circuit.
Chapter 6 presents conclusions and future perspectives.

Chapter 2

State of the art

2.1 Nanochannel Delivery System

The Nanochannel Delivery System (nDS) is an Active Implantable Medical Device (AIMD) whose purpose is to administer controlled drug doses to patients with chronic pathologies such as hypertension and rheumatoid arthritis that demand tailored and continuous therapeutic care [6]. Considering that physiological factors such as blood pressure are usually synchronized with circadian rhythms [7], the traditional approach of providing a constant dosage of drugs to address these factors is unnecessary and can lead to problems like resistance, side effects, and tolerability issues [8]. For example, medicines used to treat rheumatoid arthritis can be most effective during the 4-5 hour period of heightened nighttime immune activity, making continuous suppression of the immune system throughout the day unnecessary and unjustified [9]. nDS is provided with a silicon nanofluidic membrane, which surface charge affects the concentration of charged molecules in its nanochannels. Applying a potential between the membrane electrode and electrolyte solution allows surface charge and nanochannel charge selectivity to be controlled. Considering, for instance, a negatively charged surface, applying a negative voltage reduces the flow of negatively charged molecules by increasing the interaction layer between ions and nanochannel walls, restricting ion flow. In this way, nDS can modulate the drug release rate by applying an electric potential. It enables the continuous systemic release of the drug, achieving zero-order release kinetics that may be controlled to maintain the plasma concentration of the medicine within its therapeutic window and prevent inefficacy and harmful consequences [6]. The device includes a reservoir for the drug and a PCB responsible for controlling the all system. The PCB's dimensions are $20\,\mathrm{mm} \times 12\,\mathrm{mm}$ (Fig. 2.1), and it is composed of a low-power wireless Microcontroller Unit (MCU) (CC2640R2F), a digital temperature sensor for monitoring the environment, a membrane voltage management circuit based on a Digital Analog Converter (DAC) (MAX5532) and a 2.4 GHz antenna [10, 6]. The Bluetooth Low Energy (BLE) protocol is used to control remotely nDS thanks to the MCU. The membrane voltage can be adjusted between -3 V and 3 V for an effective tuning of the drug release. During BLE connection, it is possible to change the settings, like the voltage applied to the membrane and reading intervals of the temperature and battery level. nDS, through BLE communication, can work in two different modes. In advertising mode, it broadcasts its address for other devices, and its power consumption is of the order of a few µW. In connection mode, it is connected to another device and can send and receive data with a power consumption of a few mW. The primary battery used to power the device is the CR2016 (VARTA) with a capacity of 90 mAh. In high consumption scenario, the battery has been estimated to last 20 days before it needs to be recharged. At the current state, nDS requires periodical surgery to remove the device and recharge the battery. Therefore, a Wireless Power Transfer (WPT) strategy has been chosen to be implemented to overcome this issue.

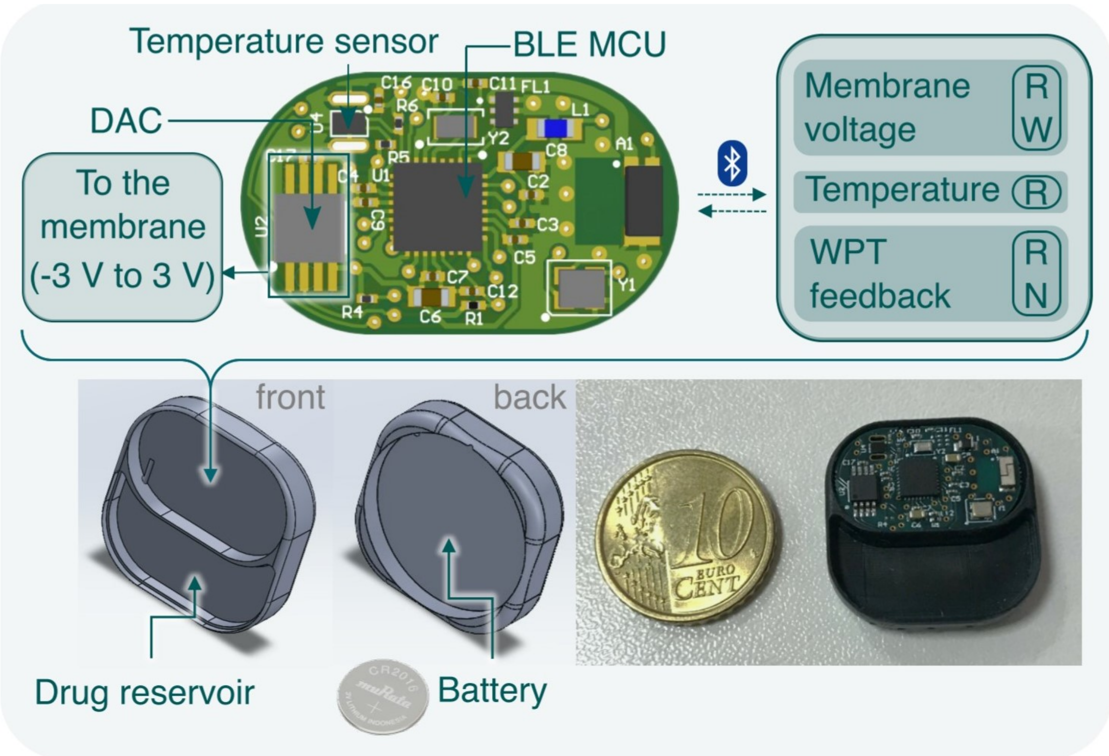

Figure 2.1: nDS Drug Delivery Device [10].

2.2 Wireless Power Transfer

The first WPT test ever conducted was by Hertz, which he intended to prove the existence of the electromagnetic wave in 1887 [11]. The experiment consisted of a transmitter (TX) dipole antenna with a spark gap that transmitted a high-voltage signal. Then, the receiver (RX) antenna produced sparks between its spark gap due to the electromagnetic energy generated by the TX antenna. Hertz proved that transmitting power without a direct connection was possible. WPT is an area of intensive research and has been adopted for various electronic products, including cell phones, robots, and electric vehicles [12, 13, 14]. WPT techniques are becoming increasingly popular in the medical field, mainly thanks to the wide use of batteries as the primary power source for AIMDs, such as nerve- and muscle-simulating systems [15], cochlear aids [16], heart pumps [17], infusion pumps [18] and pacemakers [19]. Traditional methods of charging these devices through power cables can be inconvenient because they usually need surgical intrusion or high-cost battery replacement. WPT technology provides a safe and comfortable alternative [20, 2]. However, the implementation of WPT systems in AIMDs is still challenging, since it needs to consider several parameters: the size of the WPT system, biocompatibility, heat dissipation, and efficiency. Several WPT techniques have been adopted to accomplish this challenge, including Near-Field Capacitive Coupling (NCC) [4], Near-Field Resonant Inductive Coupling (NRIC) [3], and Ultrasonic Transcutaneous Energy Transfer (UTET) [5]. The NCC technique is based on the principle of electric field coupling between two pairs of conductors (Fig. 2.2). Usually, the range of the operating frequencies of WPT systems is from hundreds of kHz to tens of MHz. This WPT method operates at high frequencies (tens of MHz) and guarantees a power transmission in a range of a few mm, with an output power of the order of hundreds of mW. It has been proved that the strength of the electromagnetic field in the human body decreases for frequencies above 100 kHz due to the increase of the absorbed energy by the tissues, translated to a rise of the body temperature [21, 22]. Hence, using the NCC method implies efficiency losses due to the tissues. In addition, the rectification needed to power a device at higher frequencies (over 30 MHz) tends to be less efficient than at lower frequencies [23]. The UTET technique uses propagating ultrasound waves to transfer power wirelessly (Fig. 2.3). In an in-vivo environment, ultrasound waves propagate through tissues to the implanted device, where a piezoelectric transducer converts the mechanical energy into electrical energy [23, 5]. The UTET method generates an output power of the order of µW, within a range of from a few mm up to about 100 mm. This technique utilizes an operating frequency range from a few hundred kHz to a few MHz. A limitation of this technique is that the acoustic impedance is not uniform in the body. For example, the acoustic impedance of the bones can be so high that all the ultrasound wave energy is reflected back;

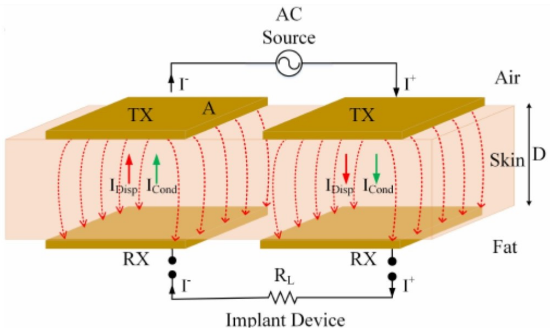

Figure 2.2: Near-Field Capacitive Coupling [23].

thus, this technique restricts the device's locations only in soft tissues with low acoustic impedance. Moreover, the long-term effects of tissue vibrations, due to ultrasound waves, can lead to adverse human safety issues [24]. The NRIC is considered the most suitable WPT strategy to meet the power requirements of AIMDs while maintaining the health of the surrounding tissue. It can transmit power more than hundreds of mW, it uses a lower range of operating frequencies than NCC and UTET (from a few hundreds of kHz to a few MHz), and it has a power transmission range similar to the skin's thickness, suitable for AIMDS (from few mm up to tens mm) [2, 23]. For these reasons, it has been chosen to implement the WPT system using the NRIC method.

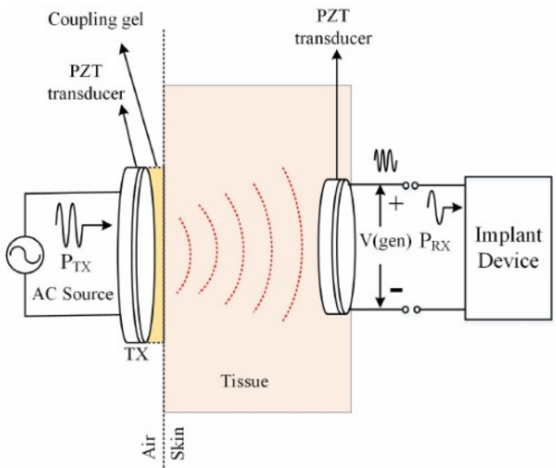

Figure 2.3: Ultrasonic Transcutaneous Energy Transfer [23].

2.2.1 Near-Field Resonant Inductive Coupling

Figure 2.4 shows the NRIC scheme. It relays on a transmitter circuit that generates an alternating current in the primary coil (TX), causing a variable magnetic field over time. This phenomenon induces an electromagnetic force (ε) on the secondary coil (RX) according to equation 2.1:

$$\varepsilon = -\frac{d}{dt}\int_{\Sigma} \overrightarrow{B}\, d\overrightarrow{A} \tag{2.1}$$

Where Σ is the surface of the RX, B is the magnetic flux density; A is the normal vector of the area [23].

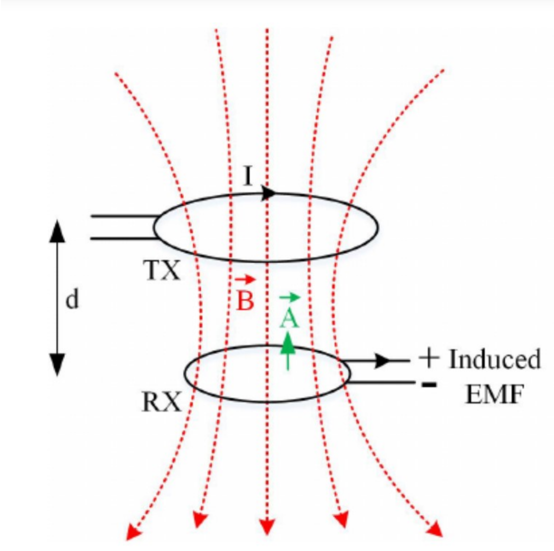

Figure 2.4: Near-Field Resonant Inductive Coupling [23].

The NRIC systems work at low frequencies (kHz range), mitigating the losses due to the tissues. These low frequencies of operation limit the distances between RX and TX to up to tens of mm; otherwise, for greater distances, the strength of the magnetic field would decrease dramatically [23]. Moreover, it is fundamental that the system is in resonance, which means that the TX and RX are tuned at the same frequency according to equation 2.2:

$$f_{res} = \frac{1}{\pi\sqrt{L_1 C_1}} = \frac{1}{\pi\sqrt{L_2 C_2}} \tag{2.2}$$

This configuration, known as resonant coupling, is used because it cancels out the RX coil reactance allowing better efficiency of the systems. There are four different types of resonant coupling: SP, SS, PS, and PP, where S is for Series, and P is for Parallel (Fig. 2.5). The power delivered in SS and SP types is the same, but how they function differs. Specifically, SS utilizes a high current and low voltage, while SP utilizes a low current and high voltage [23]. The efficiency of the rectifier used to convert alternative current (AC) to direct current (DC) is enhanced when operating with high voltage. Therefore, the SP resonant coupling method is commonly employed in biomedical applications resulting in a better conversion efficiency [25].

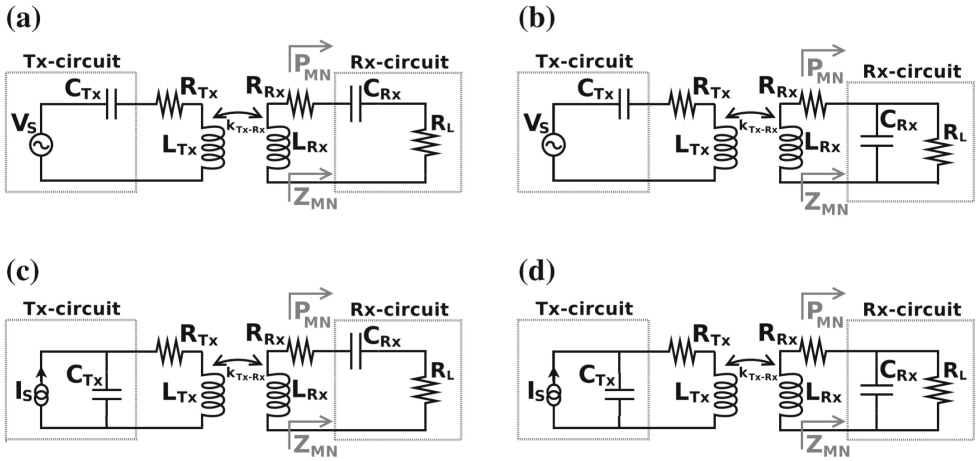

Figure 2.5: The four main configurations of resonant coupling. **(a)** Series TX and Series RX. **(b)** Series TX and Parallel RX. **(c)** Parallel TX and Series RX. **(d)** Parallel TX and Parallel RX [26].

2.2.2 Power Transfer Efficiency

The Power Transfer Efficiency (PTE) refers to the amount of power successfully transferred from the TX to the RX, compared to the total amount of power supplied to the system [27, 26]. In the NRIC system, the PTE is given by 2.3:

$$PTE = \frac{k^2 Q_{TX} Q_{RX}}{1 + k^2 Q_{TX} Q_{RX} + \frac{Q_{RX}}{Q_L}} \times \frac{1}{1 + \frac{Q_{RX}}{Q_L}} \tag{2.3}$$

Where the quality factor of the transmitter (Q_{TX}), receiver (Q_{RX}), and load (Q_L) are given by 2.4:

$$Q_{TX} = \frac{\omega_0 L_{TX}}{R_{TX}}; \qquad Q_{RX} = \frac{\omega_0 L_{RX}}{R_{RX}}; \qquad Q_L = \frac{\omega_0 L_{RX}}{R_L} \tag{2.4}$$

The Q factor is the energy loss in a resonant circuit and represents the ratio between the reactance $\omega_0 L$ and its parasitic resistance R (eq. 2.4). Higher Q factors indicate lower energy loss and greater energy storage capacity in the circuit. The coupling coefficient k represents the degree of magnetic coupling between two inductive coils [28]. The expression is shown in 2.5:

$$k = \frac{r_{TX}^2 r_{RX}^2 cos(\theta)}{\sqrt{r_{TX} r_{RX}}(\sqrt{D^2 + r_{TX}^2})^3} \tag{2.5}$$

r_{TX} and r_{RX} are the radius of the TX and RX coils, D is the distance between the coils, and θ is the misalignment angle. The coupling coefficient k is a dimensionless quantity that ranges from 0 to 1, where 0 indicates no coupling, and 1 indicates perfect coupling. From equation 2.5, it can be deduced that the case of ideal coupling is achievable when the RX and TX coils have the same radius, are perfectly co-planar, and their distance is equal to 0.

The quality factors of the TX and RX circuits and the coupling coefficient significantly impact the PTE in NRIC systems [26], as shown in equation 2.3. The Q factor of the TX and RX circuits determines the amount of power that can be efficiently transferred between the two coils. Higher Q factors result in more efficient power transfer because they reduce the losses due to resistance and increase the amount of energy that can be stored in the circuit. The coupling between the TX and RX coils also plays a critical role in the PTE of the system because when the coils are well-coupled, more of the magnetic flux generated by the TX coil links with the RX coil, leading to more efficient power transfer. The lower the PTE, the higher the energy dissipated in the RX, resulting in a higher coil temperature. For this reason, having a high PTE to limit the temperature on RX as much as possible is fundamental.

2.3 nDS Requirements

This thesis aims to develop a WPT system for nDS that can recharge the battery efficiently in an in-vivo environment. Several design requirements were considered, including optimal receiver in terms of efficiency, optimal RX coil in terms of size and efficiency, low sensitivity to any misalignments in the RX coil, low heat dissipation, the reliability of the charging process, and high PTE. Although the PTE is an important metric for the evaluation of WPT systems [26], the design of the system was more focused on biocompatibility (low heat dissipation requirement) and the reliability of the charging process. For the receiver investigation, commercial receivers, such as LTC4124 and LTC4126, were tested and compared. For the requirement of an optimal RX coil, coils with a diameter from 6 mm up to 19 mm were tested. Although making the device as small and unobtrusive as possible would be preferable, a smaller RX coil diameter would result in a lower coupling coefficient, decreasing the PTE and increasing the heat production for the same power transmitted. Moreover, as the implanted device in an in-vivo test will likely not be perfectly aligned with the transmitter, the selected RX coil needs to ensure that any variations in efficiency are not significant. To meet these needs, the system was designed based on a closed-loop using BLE communication developed by Bontempi and Del Bono [29, 10]. The RX informs the TX when to adjust the power transmitted based on the power absorbed by RX. This mechanism maintained steady and appropriate power transmission, preventing the coil from overheating due to excess power.

2.4 Receiver LTC4124

The LTC4124 is a wireless Li-Ion charger that can receive power wirelessly from an alternating magnetic field created by a TX coil [30]. Figure 2.6 shows the functional block diagram of the LTC4124. It needs an external parallel resonant LC tank connected to the ACIN pin to allow the device to receive power wirelessly. This device has a diode, a comparator, and switches that help to regulate the rectified voltage on the VCC pin. Diode D1 is used to rectify the AC voltage at the ACIN pin, and the comparator CP1, switches SW1 and SW2 work together to regulate the rectified voltage on the VCC pin. During the recharge phase, they ensure that the voltage on the VCC pin is between 0.85 V and 1.05 V above the voltage on the BAT pin. When the charging process is completed, the Ideal Diode Control block, together with the Charger Control block, drive the gate M2 and M1, shown in the block diagram (Fig. 2.6), to achieve a low voltage drop (50 mV) from the BAT pin to the VCC pin. To ensure that the VCC pin achieves a voltage level that closely matches the BAT pin, the current is directed from the BAT pin to the VCC pin. On the contrary, in charging mode, the current is directed from the VCC pin to the BAT pin.

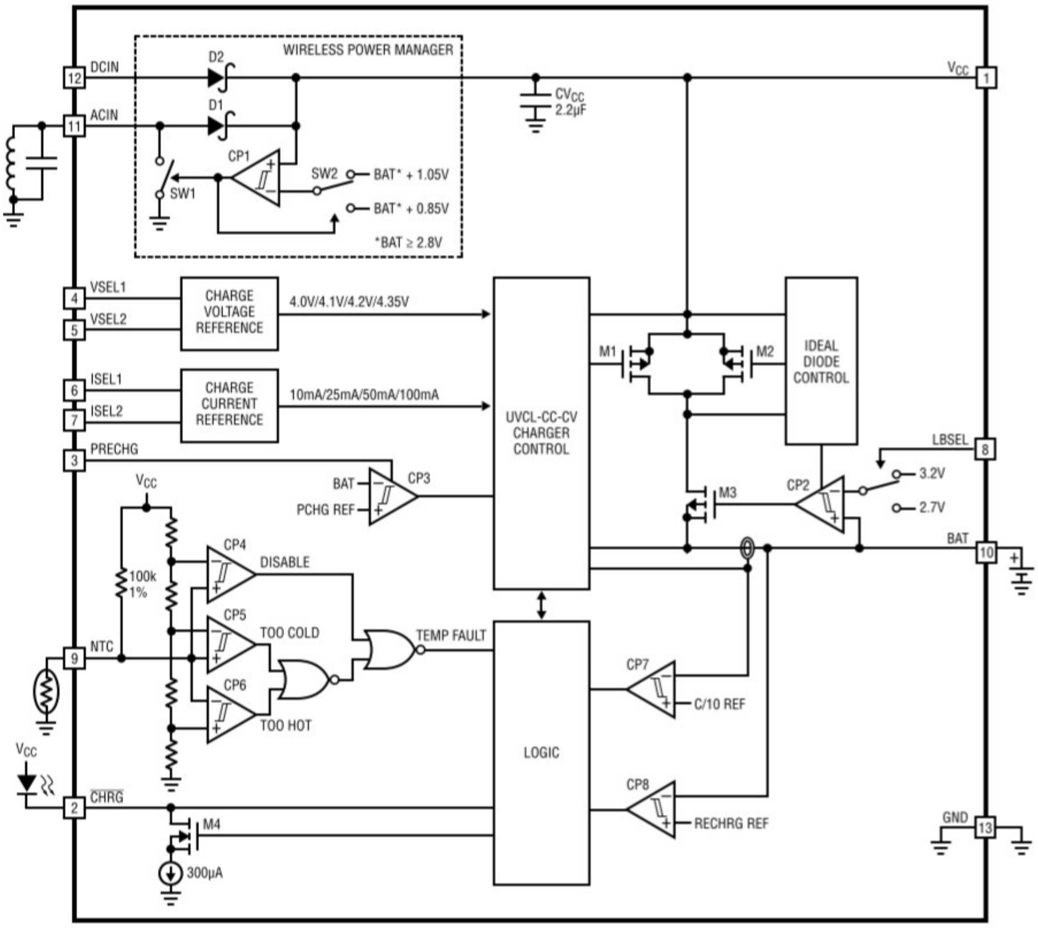

Figure 2.6: Functional block diagram of the receiver LTC4124 [30].

2.4.1 Li-Ion Charger Controller

The LTC4124 also includes a constant current and constant voltage CC/CV linear battery charger with several safety features, including a timer termination, bad battery detection, and Under-Voltage Current Limiting (UVCL). The charging process is carried out in CC/CV mode, typical for Li-Ion battery charging. Figure 2.7 shows the ideal CC/CV curve. In the CC mode, the voltage exhibits a linear growth pattern. Meanwhile, the current remains constant at I_{CHRG} until the voltage exceeds the recharge threshold, which is typically set at 97.6% of the V_{CHRG}. At this stage, the recharging process passes to the CV mode, where a constant voltage is applied, while the current gradually decreases, as depicted in figure 2.7. In CC mode, the CHRG pin blinks slowly (0.8 Hz), indicating that the LTC4124 is powered on and charging the battery. When the battery reaches the V_{CHRG}, the CHRG pin stops blinking and is pulled down and a timer is activated, interrupting the charging process precisely after 3 hours. The LTC4124 allows the user to select the charge current (I_{CHRG}) and the charge voltage (V_{CHRG}) at which the battery is considered wholly charged. The selection requires only connecting the ISEL 1/2 and VSEL 1/2 pins to VCC or ground.

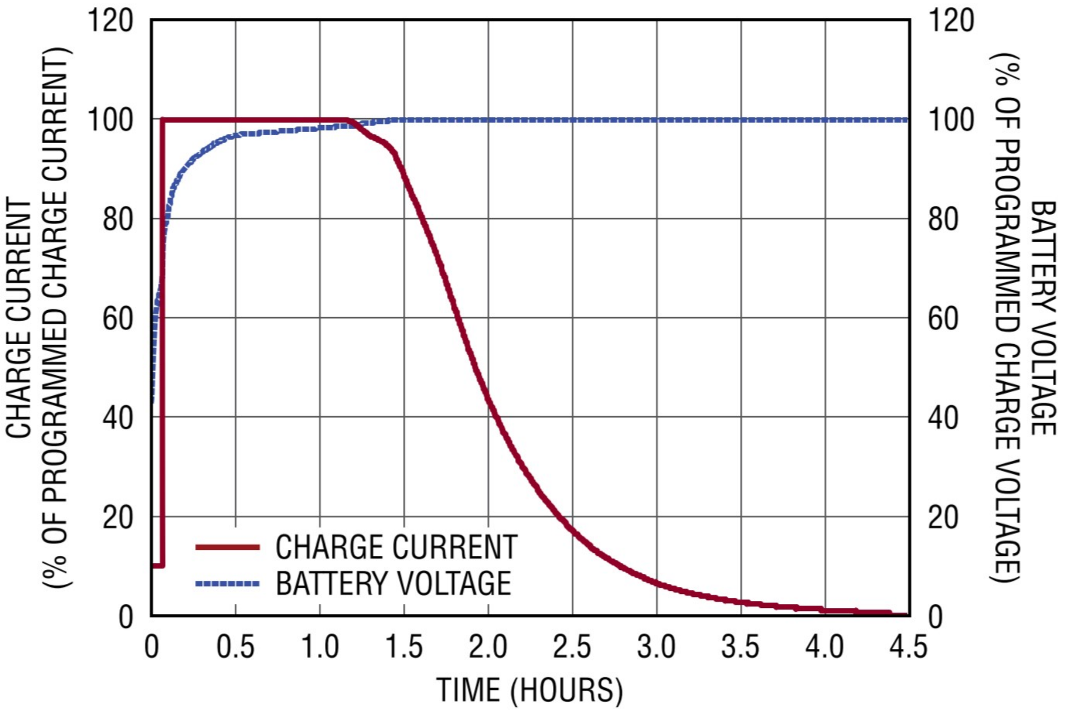

Figure 2.7: Charge Current vs Battery Voltage in a charging cycle with Pre-Charge enabled [30].

2.4.2 Under Voltage Current Limiting

If the voltage on the VCC pin is less than 3.4 V, the UVCL implemented in the LTC4124 decreases the current delivered to the battery towards zero. This feature is particularly useful in situations where the coupling between the TX and RX coils is weak; thus, the available power is limited. Without this function, the VCC voltage may fall below the minimum operating voltage (2.7 V) when the charger attempts to deliver the full I_{CHRG}. In this case, the LTC4124 would immediately interrupt the I_{CHRG}, causing the VCC voltage to rise above the minimum operating voltage and restarting the charger. This back-and-forth pattern would cause irregular charging. The UVCL feature overcomes this undesired behavior by gradually adjusting the I_{CHRG} as the input power level varies. When a UVCL fault is detected (VCC < 3.4 V), the I_{CHRG} is reduced gradually to zero and the CHRG pin starts to blink fast (6 Hz).

2.4.3 Pre-Charge Mode and Low Battery Disconnect

The LTC4124 implements a Low Battery Disconnect feature to protect the battery from over-discharging, which is fundamental for not reducing the battery's life. When VBAT reaches a voltage below the selected disconnected battery voltage ($V_{BAT-LBDIS}$), the LTC4124 is switched off, interrupting any current consumption from the battery. The $V_{BAT-LBDIS}$ can be programmed to 2.8 V or 3.2 V through the pin LBSEL. The LTC4124 has also a pre-charge mode that can be enabled or disabled by the PRECHRG pin. When the battery has been deeply discharged, reaching a value below the $V_{BAT-LBDIS}$, this mode is used for recharging. Enabling the pre-charge mode starts the delivery of the 10% of the I_{CHRG} until the battery voltage exceeds the threshold set at 68% of the V_{CHRG}, as shown in figure 2.7. If the battery has not exceeded the 68% of the V_{CHRG} threshold after the bad battery detection time (t_{bb}), the CHRG pin blinks fast (6 Hz) to indicate that the battery is faulty.

2.4.4 Temperature Qualified Charging

The LTC4124 is also provided with an NTC pin, used for the Temperature Qualified Charging feature, which ensures that the recharging process is carried out within safe battery temperature limits. Comparators CP5 and CP6, shown in figure 2.6, detect the upper and lower threshold of the battery temperature by evaluating the voltage on the NTC pin (V_{NTC}). By connecting a 100 kΩ NTC (Negative Temperature Coefficient), the upper threshold (cold threshold) is set at 75% of VCC, while the lower threshold is at 35% of VCC (hot threshold). When V_{NTC} exceeds these limits, the charging process is interrupted, reducing the I_{CHRG} to zero and making the CHRG pin blinking fast (6 Hz) to indicate a battery temperature fault. This feature can also be disabled by connecting the NTC pin directly to VCC.

2.4.5 Recharge Status Indicator

The CHRG pin is an open drain pin designed to indicate the status of the charging process. This pin is connected to an internal 300 µA pull-down current, allowing to connect a led to indicate status conditions. Table 2.1 summarizes the led frequencies according to the recharge status condition.

LED	**Recharge Status**
High Impedance	No Input Power
Blink Slow (0.8 Hz)	Powered On and Charging
Blink Fast (6 Hz)	Battery Temperature Fault or Bad Battery Detected Fault or UVCL Fault
Pull Down	Charging Complete

Table 2.1: Recharge States Table [30].

2.5 Receiver LTC4126

The LTC4126 is a wireless Li-Ion battery charger, similar to the LTC4124, with an incorporated step-down DC/DC converter [31]. Figure 2.8 shows the functional diagram block. Its purpose is to facilitate the wireless charging of mobile devices and deliver a 1.2 V output, which is well-suited for supplying power to a hearing-aid Application-Specific Integrated Circuit (ASIC). The component comprises three main circuit elements: an AC power controller, a comprehensive linear battery charger, and a step-down DC/DC converter.

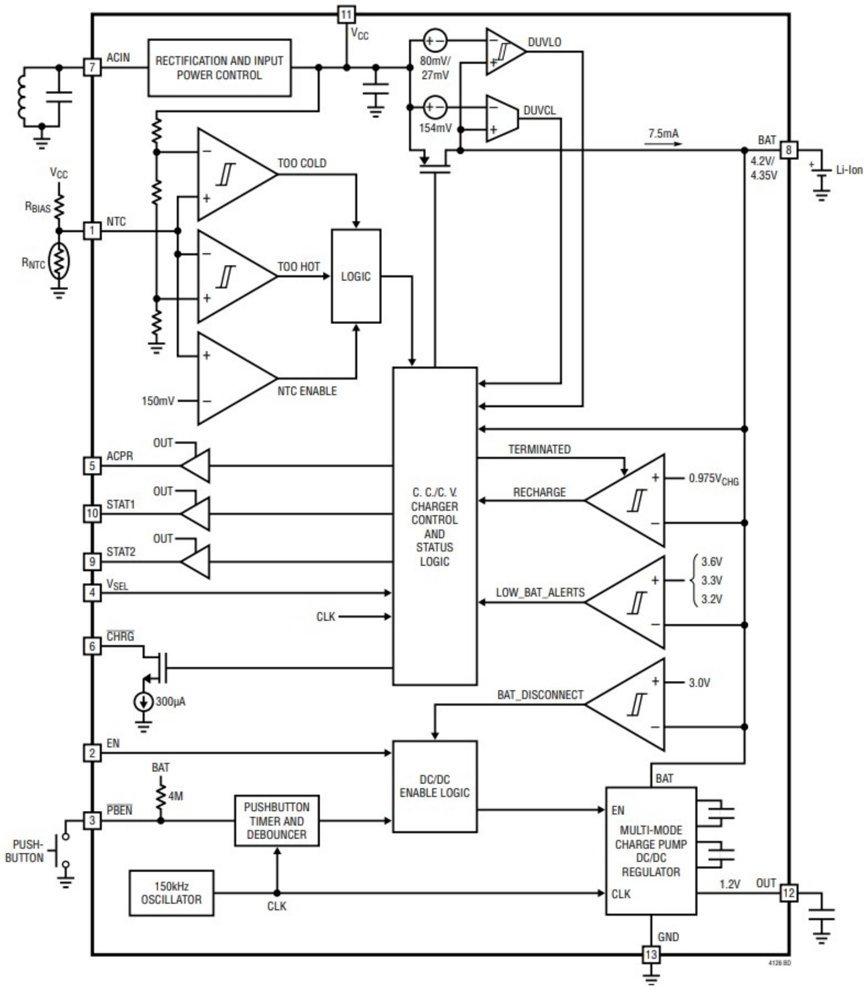

Figure 2.8: Functional block diagram of the receiver LTC4126 [31].

2.5.1 AC Power Controller

The LTC4126, as a receiver, needs to be equipped with an external parallel resonant LC tank connected to the ACIN pin. By employing this configuration, the LTC4126 can efficiently receive wireless power from an alternating magnetic field produced by a TX coil. To convert and regulate the received power, the Rectification and Input Power Control circuitry, depicted in the functional diagram block (Fig. 2.8), performs two key functions. Firstly, it rectifies the AC voltage present at the ACIN pin. Secondly, it regulates the rectified voltage at the VCC pin, ensuring it remains below a fixed threshold of 5.5 V.

2.5.2 Linear Battery Charger and Features

The LTC4126, like the LTC4124, as a wireless Li-Ion battery charger, performs the charging process in both CC and CV modes. It has functionalities such as automatic recharge, safety timer-based termination, detection of faulty batteries, and the Temperature Qualified Charging feature. The charge current (I_{CHRG}) is internally set at a fixed rate of 7.5 mA, and the final charge voltage (V_{CHRG}) can be selected between 4.2 V or 4.35 V using the VSEL pin, where the logic pin high selects the 4.35 V and the logic pin low selects the 4.2 V. As shown in figure 2.9, when the voltage differential between the VCC pin and the BAT pin exceeds by approximately 80 mV, the charger initiates the charging process. At the beginning of the recharge, a termination timer of 6 hours is activated. When the voltage differential rises above approximately 154 mV, the charger switches to CC mode, delivering the full I_{CHRG} to charge the battery. Figure 2.10 shows a typical Li-Ion battery charge profile using the LTC4126. As the BAT pin voltage reaches V_{CHRG}, the charger transitions to CV mode, gradually reducing I_{CHRG}. The current continues to decrease while maintaining the BAT pin voltage at the desired V_{CHRG}. Upon completion of the 6-hour termination timer, the charging process is considered complete. To initiate a new charging cycle, it is necessary to disconnect and reconnect the power source at either ACIN or VCC or if the battery remains connected long enough, the charger will draw 3.7 µA and a new cycle will be started as soon the battery falls below 97.5% of V_{CHRG}. At the end of the 6-hour charge cycle, if the battery fails to attain a voltage higher than V_{CHRG}, the battery is considered faulty. The Temperature Qualified Charging feature of the LTC4126 has the same purpose of ensuring the charging process is performed with safe battery temperature limits. Unlikely the LTC4124, the LTC4126 needs to connect a resistor between VCC and the NTC pin and an NTC thermistor connected between the NTC pin and ground to create a voltage divider for V_{NTC}. Meanwhile, the two comparators, shown in the functional block diagram 2.8, set the hot threshold at 34.9% of VCC and the cold threshold at 76.5% of VCC. If the battery temperature exceeds one of these limits, the charging process is interrupted.

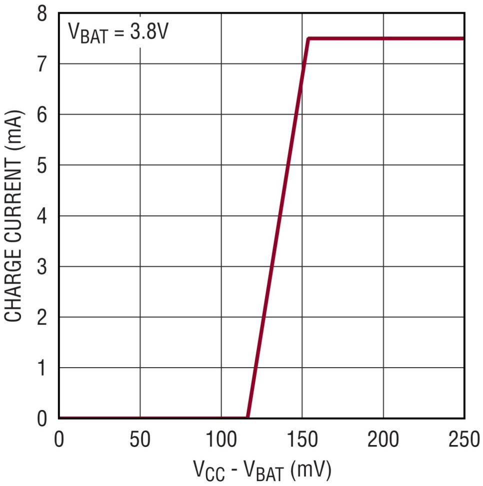

Figure 2.9: I_{CHRG} vs VCC-VBAT [31].

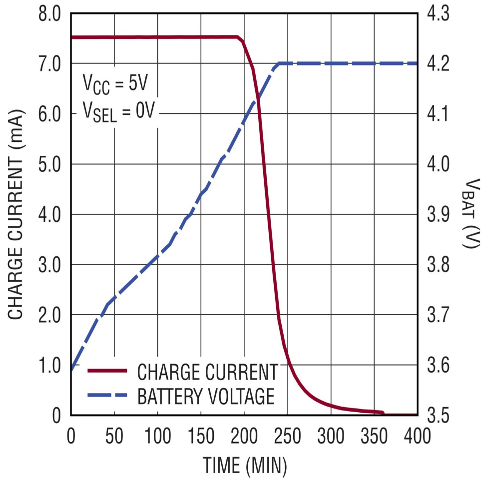

Figure 2.10: Battery charge profile [31].

2.5.3 Step-Down DC/DC Converter

The LTC4126 is designed to deliver power from the battery to the system load through the OUT pin. To accomplish this, the IC incorporates a low-noise multi-mode charge pump DC/DC converter, which can be enabled by applying a minimum voltage of 1.1 V to the EN pin. The converter can operate concurrently with the charger to ensure that the system load is always powered on. The DC/DC converter works in different modes, dictating the charge pump's switching frequency configuration. In these modes, the switching frequency of the charge pump can be set to either 50 kHz or 75 kHz. The OUT pin is studied to power the hearing aid ASIC. Therefore, these particular frequencies are deliberately chosen to ensure that any noise remains outside the audio frequency range, preventing interference. The charge pump DC/DC converter offers three different modes of operation, which are determined by the VBAT as shown in figure 2.11.

In Mode 1, when VBAT exceeds 3.6 V, it functions as a 3:1 step-down converter and provides a regulated 1.2 V output. The internal current limit circuitry ensures that the maximum output current of the converter is approximately 65 mA. In Mode 2, when VBAT falls within the range of 3.6 V to 3.3 V, the charge pump continues to operate in Mode 1. However, it can no longer maintain 1.2 V of output regulation. Instead, it delivers a maximum of one-third of VBAT. This mode can be modeled using the Thevenin equivalent circuit shown in figure 2.12. To calculate the output voltage (V_{OUT}) for a specific load current (I_{OUT}), the following equation (2.6) can be used:

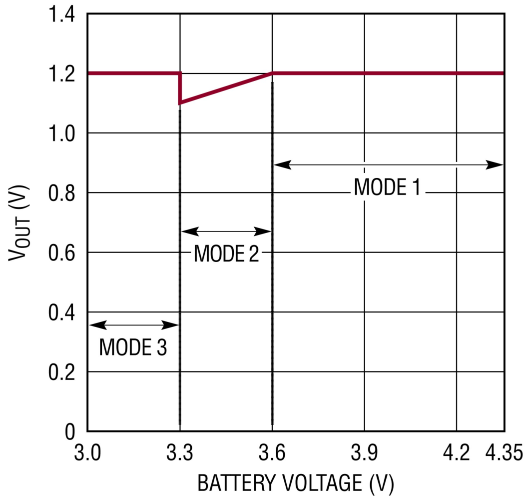

Figure 2.11: Operational Modes DC/DC converter [31].

$$VOUT = \frac{VBAT}{3} - I_{OUT} \cdot R_{OL} \tag{2.6}$$

Where the effective output resistance (R_{OL}) typically measures 4.6 Ω at room temperature. R_{OL} may vary depending on factors such as battery voltage, switching frequency, and temperature. In Mode 3, when VBAT drops below 3.3 V, the converter operates as a 2:1 step-down converter and maintains a regulated 1.2 V output. In this mode, the maximum I_{OUT} of the DC/DC converter decreases until an approximately level 35 mA.

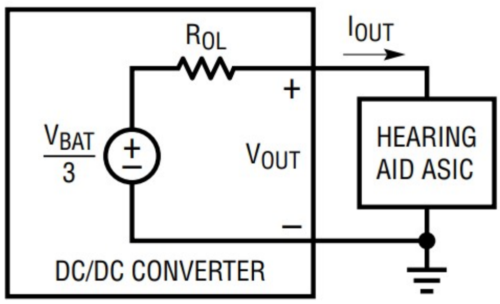

Figure 2.12: Mode 2 Thevenin equivalent circuit [31].

2.6 Closed-Loop WPT system

The WPT system was designed based on a closed-loop using BLE communication developed by Bontempi and Del Bono [29, 10] to ensure the reliability of the charging process. In these works [29, 10], the NRIC link was tested using the evaluation kit (DC2770A), which contained two integrated circuits. One is the LTC4124 as RX, and the second is the LTC4125 as TX (Fig. 2.13). The LTC4124 employs an external parallel resonant LC tank. The RX coil used is the 760308101220 (Wurth Electronic), and it has a diameter of 17 mm and a thickness of 0.8 mm, with an inductance of 12.6 µH. A capacitor of 0.047 µF is employed to obtain a resonant frequency of 200 kHz, with a quality factor of 25 at this frequency. On the other hand, the LTC4125 uses one coil in series with two capacitors in parallel. The coil used in this case is 760308101104 (Wurth Electronic), with a diameter of 20.8 mm, an inductance of 6.8 µH, and a thickness of 2.8 mm. Two capacitors in parallel are utilized ($C_{TX1} = 0.068\,\mu F$ and $C_{TX2} = 0.022\,\mu F$) to achieve almost the same resonant frequency as the RX [32]. The quality factor of the TX coil at this frequency is 60.9.

Figure 2.13: The transmitter LTC4125 and the receiver LTC4124 [32].

The performance of the system was tested in terms of overall efficiency according to 2.7:

$$\eta_{Tot} = \eta_{TX} + \eta_{PTE} + \eta_{RX} \tag{2.7}$$

η_{Tx}, η_{PTE}, η_{RX} are not trivial parameters to calculate. Thus, it was used an equivalent formulation of the overall efficiency (equation 2.8):

$$\eta_{Tot} = \frac{P_L}{P_{TX}} \tag{2.8}$$

Where P_L is the sum of P_{Bat} and P_{nDS}.

In these conditions, the evaluation board of the LTC4125 was modified to develop a closed-loop system that ensures a consistent power transmission without interruptions. Figure 2.14 presents a scheme of the WPT system using the closed loop. Two MCUs, one for the TX and one for the RX, were used. The TX is controlled by the LAUNCHXL-CC2640R2, which sets the power transmission level according to the data sent by the RX. The RX is controlled by the MCU of nDS (CC2640R2F), which reads the data from the RX and, according to an algorithm, sends a message to the TX to whether increase, decrease or maintain the power level. The MCU of nDS requires at least 3 V as power supply (V_{nDS}). Therefore, a buck-converter (TPS82740B) was introduced to regulate the VCC to a steady 3 V. During the tests to evaluate the system, the battery LIR2025 was used with a selected I_{CHRG} of 10 mA and a selected V_{CHRG} of 4.2 V. This section presents the main modifications and the main features of the LTC4125, alongside the developed algorithm to control the closed-loop WPT system.

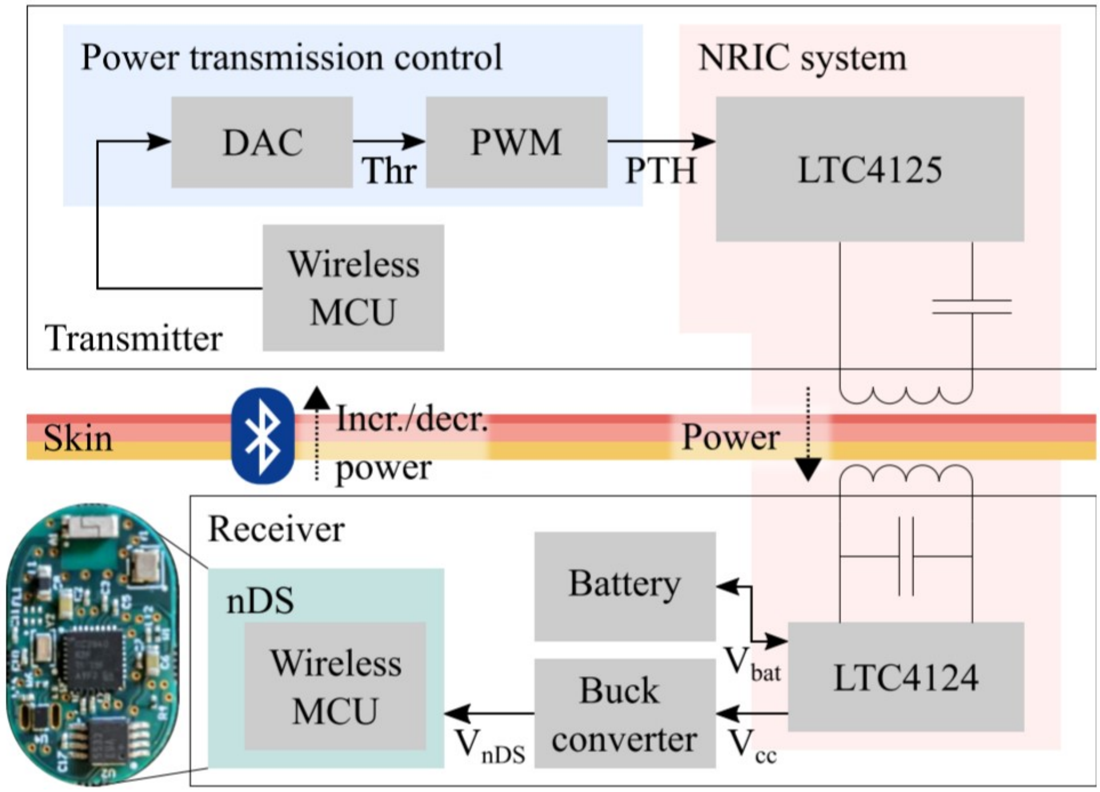

Figure 2.14: Closed-Loop WPT system [10].

2.6.1 Transmitter LTC4125

The LTC4125 is an Integrated Circuit (IC) designed to be a wireless power transmitter by providing three main features: Optimum Power Search algorithm, AutoResonant function, and Foreign Object Detection [33]. The AutoResonant function ensures the resonance coupling between the TX and RX, the Optimum Power Search algorithm maximizes overall PTE, and the Foreign Object Detection ensures safe and reliable operation when working in the presence of conductive foreign objects. Figure 2.15 shows the functional block diagram of LTC4125.

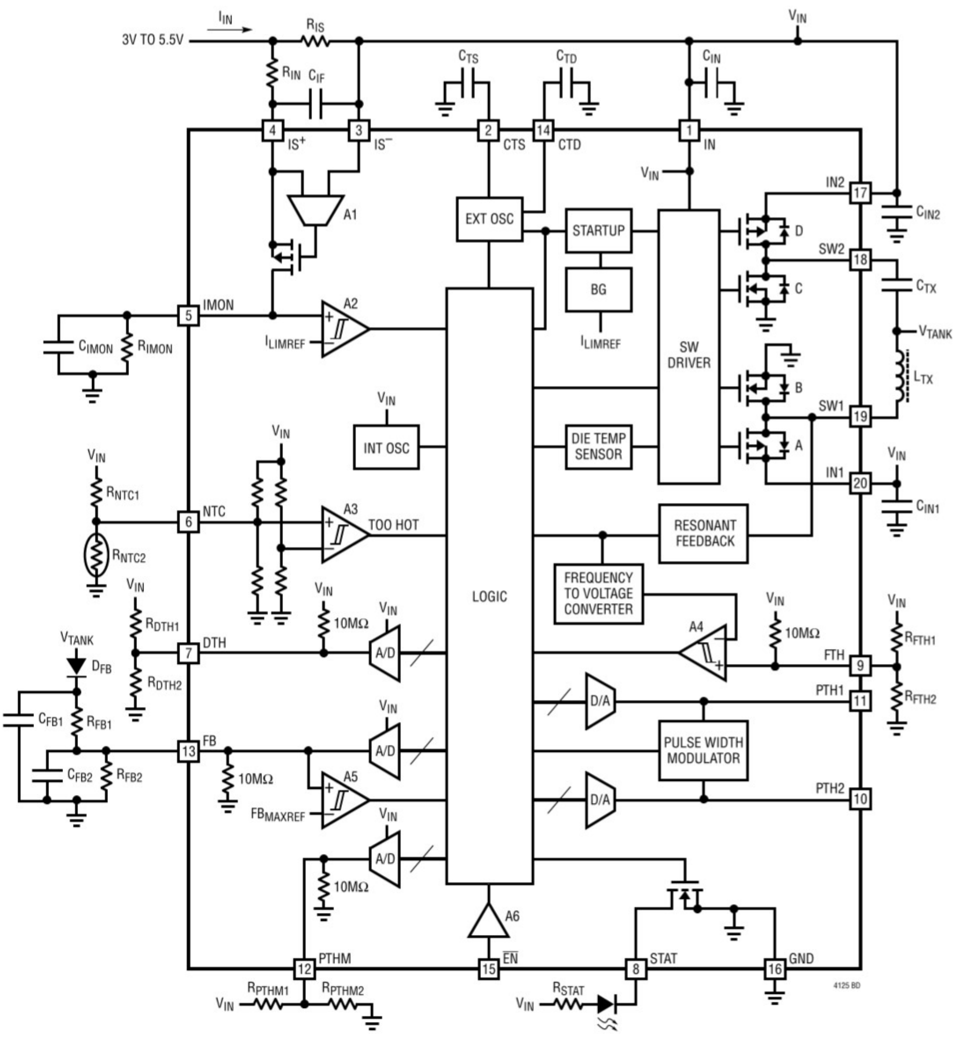

Figure 2.15: Functional block diagram of the transmitter LTC4125 [33].

2.6.2 Optimum Power Search and Modifications

The Optimum Power Search algorithm is a feature of the LTC4125 designed to overcome the variability of the transmission conditions and, most importantly, to detect a valid RX [33]. The full-bridge driver generates a square wave on the SW pins, and the algorithm modifies the pulse width of this wave. By doing so, the algorithm can regulate the amplitude of the current flowing through the coil, as shown in figure 2.16, and thus control the strength of the magnetic field. Therefore, changing the pulse width means changing the power delivered to the RX.

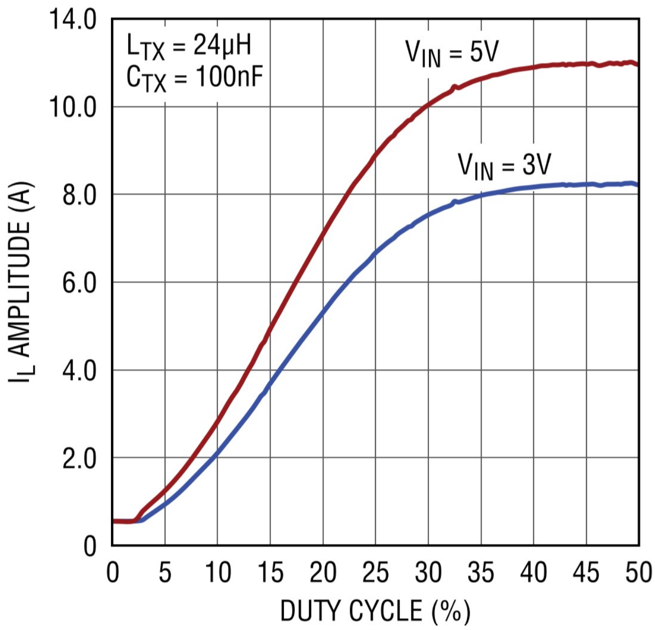

Figure 2.16: Coil Current vs Duty Cycle [33].

The Optimum Power Search algorithm (Fig. 2.17) is divided into three distinct phases. During the first phase (T1), the device transmits power at its starting value chosen by the voltage applied to the PTHM pin. During the second phase (T2), a step-wise linear ramp of transmit power is applied. The pulse width increases the power level transmitted at each step to search for the RX. In this phase, two outcomes are possible: a positive search or a negative search. If a positive search is detected, the third phase (T3) is reached, and the power transmitted remains constant. On the other hand, in case of a negative search, the device is forced to continue to increase the pulse width until it reaches 50% of the duty cycle; at this point, the power transmission drops to zero, and the LTC4124 returns to phase T1.

The LTC4125 implements primary and secondary exit conditions to identify a valid RX during phase T2. The primary exit condition is not programmable, while secondary ones can be programmed via hardware. The primary condition triggers the exit from phase T2 by evaluating the peak LC tank voltage from the FB pin. The search process terminates once the LTC4125 detects a significant variation in the LC tank. At this point, the transmit power is maintained at the current level until the start of the next search interval. The two programmable secondary exit conditions are the Input Current Threshold (ITH) and the Differential Tank Voltage Threshold (DTH).

Any fault condition causes the pulse width to be reduced to zero and the restarting of the Optimum Power Search algorithm. There are six fault conditions that the device can detect: Foreign Object Detection (detected by the frequency threshold set by the FTH pin), excessive coil temperature (detected by the NTC pin), excessive tank voltage (detected by the feedback FB pin), end of search ramp, input current limit (detected by the IMON pin), and internal (die) over temperature.

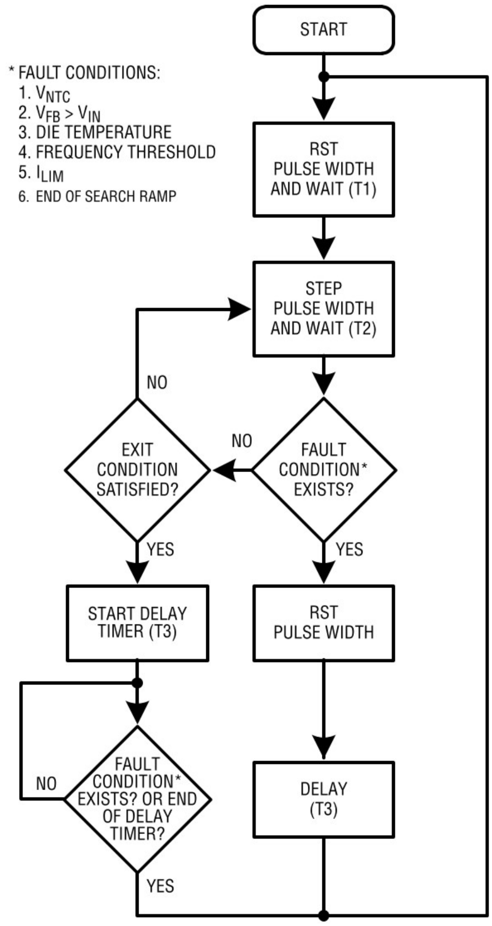

Figure 2.17: Optimum Power Search algorithm flow chart [33].

In this application, the term "open-loop" means the evaluation of the peak LC tank voltage, which is used as the primary exit condition in the optimum Power Search algorithm. In contrast, the term "closed-loop" refers to a control loop that actively involves both the TX and RX. During Bontempi and Del Bono testing, it was found that the primary exit condition of the TX was not accurate enough in open-loop control [29, 10]. The TX relies on the V_{FB} to determine the presence of the RX during the Optimum Power Search phase. However, the small variation of the FB signal between the two steps can be insufficient to detect the presence of the RX. This results in the power transmission dropping to zero, leading to unreliable recharge. To address this problem, two possible solutions were considered. The first solution involved using the DTH pin to establish a secondary exit condition based on a voltage step size threshold [33]. This solution can be used when the NRIC link is at the lowest coupling condition. However, it may not be optimal if the transmission condition varies, as a fixed threshold could lead to inadequate power transmission. The second solution proposed was to use a closed-loop system to bypass the FB pin. Employing a closed-loop system, where the power transmission is managed according to the RX's requirements, would overcome the problems due to the step size of the FB pin. This solution is the most suitable since changing the voltage on the PTH pin would be sufficient to modify the transmitted power (eq. 2.12). Closed-loop control has several advantages over open-loop control. The RX provides feedback to the TX, which adjusts the transmitted power accordingly. This results in better PTE, a reliable recharge process, and lower heat dissipation in both TX and RX coils, since the TX can adapt to changes in transmission conditions.

Three modifications were made to the LTC4125 board of the evaluation kit DC2770A [29, 10] to develop a closed-loop control for the WPT system. The first modification involved the IMON pin, which activated the secondary exit condition during phase T2. The second modification was made to the PTHM pin. The third modification was the creation of a new circuit for controlling power transmission using the PTH pin.

2.6.3 Input Current Monitoring

The LTC4125's architecture, as depicted in figure 2.15, utilizes three pins, namely IS-, IS+, and IMON, to monitor the input current [33]. The input current parameters, input current threshold (ITH), and input current limit (ILIM), are monitored using a combination of resistors RIS, RIN, and RIMON. The current flowing through the sense resistor RIS can be monitored by measuring the voltage across the IMON pin using the following formula 2.9:

$$V_{IMON} = \frac{R_{IMON} \cdot R_{IS}}{R_{IN}} \cdot I_{RIS} \tag{2.9}$$

The ITH is one of the secondary exit conditions in the Optimum Power Search algorithm, and it is set using resistors RIS, RIN, and RIMON according to equation 2.10:

$$I_{TH} = \frac{R_{IN}}{R_{IMON}} \cdot \frac{V_{ITH}}{R_{IS}} \tag{2.10}$$

V_{ITH} is referred to as VIMON at 0.8 V. During phase T2 of the Optimum Power Search, if the input current surpasses the threshold ITH the search process will halt, and the LTC4124 will maintain the pulse width until the next search interval. The IMON pin also detects one of the fault conditions, the ILIM, as per equation 2.11:

$$I_{LIM} = \frac{R_{IN}}{R_{IMON}} \cdot \frac{V_{ILIM}}{R_{IS}} \tag{2.11}$$

V_{ILIM} is typically 1.25 V. When the input current surpasses the ILIM threshold at any moment during operation, power transmission is interrupted, and the pulse width is reduced to zero until the subsequent search interval. The ILIM is usually set to 150% of the ITH, ensuring that the LTC4125 is protected against overloading, damaging the device. Even if ILIM is reached after a valid exit condition is found, transmit power is reduced to zero and maintains this level until the next search interval. The first modification involved the addition of a voltage divider between V_{IN} and ground. The voltage at the IMON pin was fixed at a higher voltage with respect to V_{ITH}, which forces the Optimum Power Search algorithm to detect a positive search immediately when the TX reaches phase T2 passing to phase T3 [29, 10]. Figure 2.18 illustrates the results of the change in the Optimum Power Search algorithm. The positive search, after modification, shows the exclusion of phase T2. The Optimum Power Search begins with phase T1, then the PTH pin increases by only one step of 75 mV, overcoming phase T2 and immediately reaching phase T3.

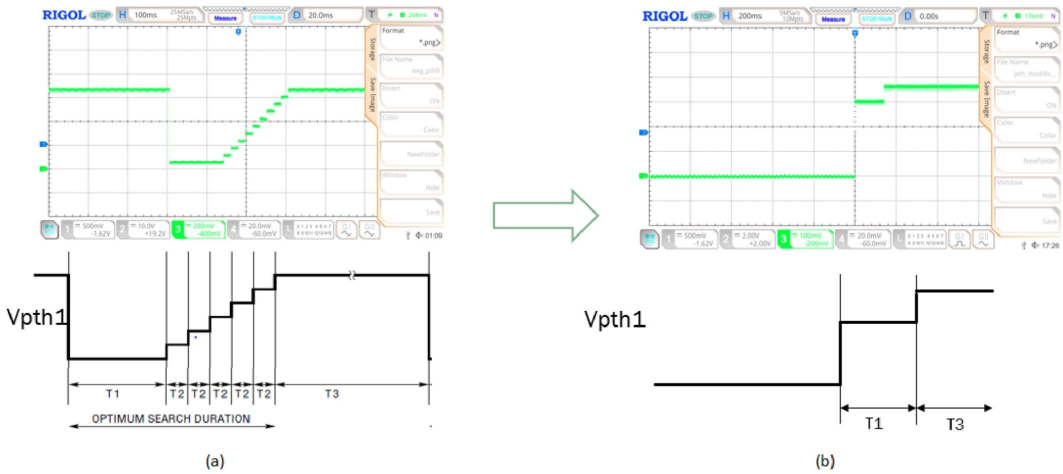

Figure 2.18: a) PTH voltage before IMON modification. b) PTH voltage after IMON modification [29].

2.6.4 PTHM and PTH Circuit

The pulse width determines how much power the LTC4125 will transmit to the RX [33]. Hence, the LTC4125 is designed to allow the monitoring of the pulse width. This is achieved by measuring the voltage on the PTH1 and PTH2 pins, which are proportional to the pulse width, as per equation 2.12, where f_n is the resonant frequency of the LC tank.

$$PW_{SW_x} = (\frac{0.24}{f_n} \cdot V_{PTH_x}) + 150ns \tag{2.12}$$

During the T2 phase, the pulse width gradually increases, resulting in a corresponding increase in the voltage on the PTHx pin. However, only one PTH pin is available for monitoring, as only half of the full bridge can be used. On the other hand, in the T1 phase of the Optimum Power Search, the voltage at the PTHM pin determines the initial pulse width, as described in equation 2.13.

$$MINPW = (\frac{0.576}{f_n} \cdot \frac{V_{PTHM}}{V_{IN}}) + 150ns \tag{2.13}$$

The V_{PTHM} is programmable through a voltage divider between V_{IN} and ground. At the beginning of the power search, the initial value of the PTH pin is determined by the PTHM pin, according to equation 2.14, as it determines the initial pulse width.

$$V_{PTH_x} = \frac{0.576 \cdot V_{PTHM}}{0.24 \cdot V_{IN}} \tag{2.14}$$

The second modification involved the initial value of PTH. Instead of setting the initial value of the PTH pin to the minimum in phase T1 (as the PTHM pin was connected to ground in the evaluation board [32]), the PTH pin was set to a higher initial value determined by the voltage divider at the PTHM pin. This ensured that the TX started at the appropriate power level, improving the overall efficiency of the system [29, 10].

Figure 2.19 shows the PTH circuit implemented as the third modification [29, 10]. Although the PTH pin is not properly an input pin, it was used as an input, since it controls the pulse width of the control signal of the TX LC tank (eq. 2.12). An N-MOSFET (TN0702) in series with an external pull-down resistor was used to discharge a capacitor connected to the PTH pin. By toggling the N-MOSFET on and off using a control signal, the capacitor can be discharged or charged, modifying the voltage at the PTH pin and thus controlling the power transmission.

A feedback circuit was devised to regulate the N-MOSFET, which comprised a comparator (TLV7011) and a DAC (MAX5532EUA). The comparator evaluates the capacitor voltage compared to the threshold set by the DAC. When the capacitor voltage exceeds the high threshold, the comparator output becomes high. This drives the gate of the N-MOSFET into saturation, enabling the capacitor to discharge. Conversely, when the capacitor voltage fall below the low threshold, the comparator output drops to zero. This causes the N-MOSFET to enter the interdiction state, enabling the charging of the capacitor. In this way, V_{PTH} is forced to follow the threshold set by the DAC. The PTH circuit allows the MCU of the TX to regulate the power transmission by changing the DAC output value.

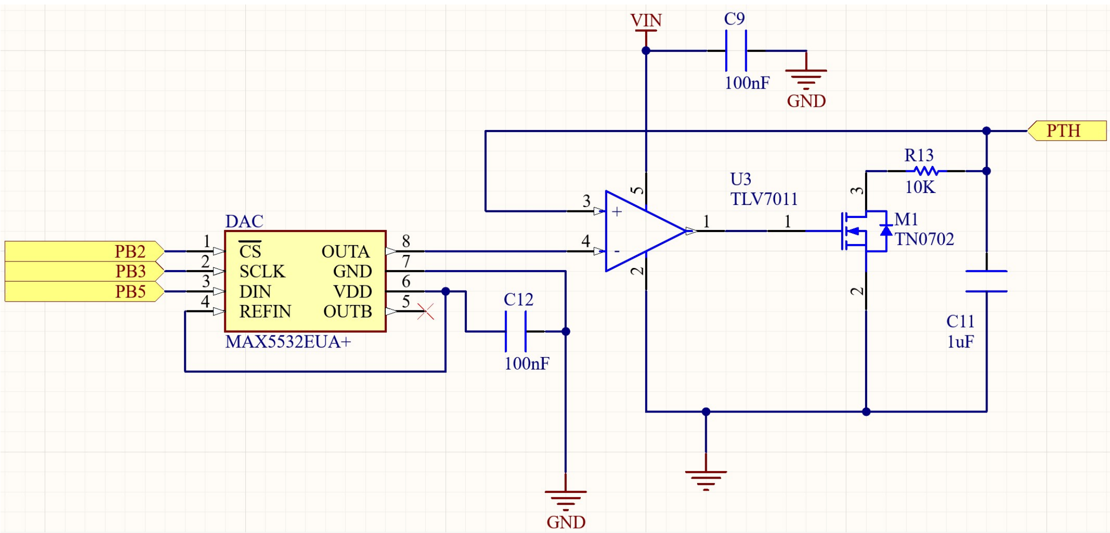

Figure 2.19: PTH circuit.

2.6.5 AutoResonant Function

The AutoResonant function is a crucial aspect of the LTC4125 that ensures power delivery always under resonance conditions [33]. This feature employs a square wave voltage source at 2.5 kHz to drive the LC tank at startup. As current flows in the LC tank, the frequency of the input voltage is adjusted by the LTC4125 to ensure that the voltage and current waveforms across the inductor and the capacitor are in phase, achieving the resonance frequency of the LC tank as shown in figure 2.20. This method to control the frequency cycle by cycle guarantees that the LTC4125 always drives the external LC tank at its resonant frequency, even with continuously changing variables such as temperature and the reflected impedance of a nearby RX. As a result, the AutoResonant function allows the WPT system to have optimal PTE by working under resonance coupling conditions.

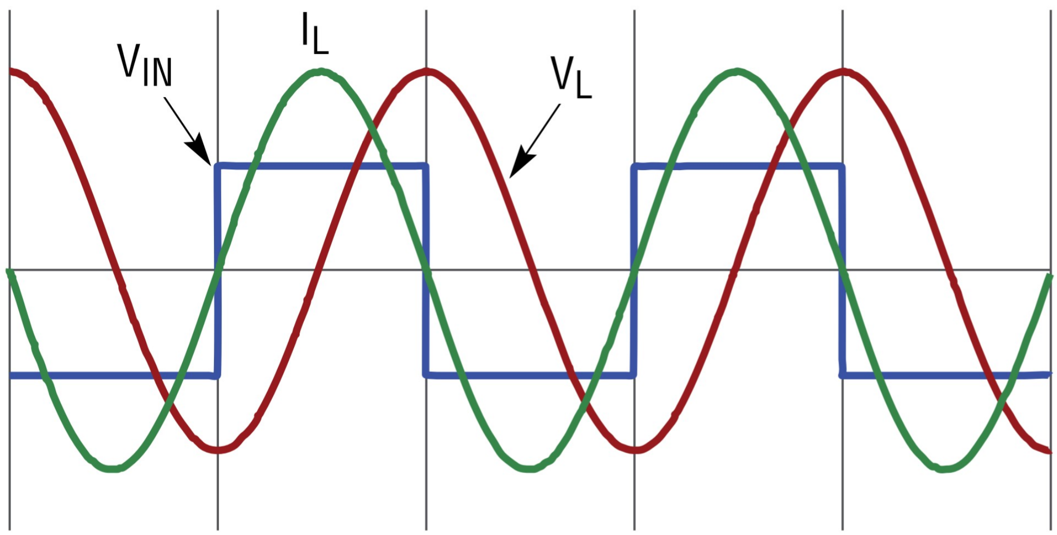

Figure 2.20: LC Tank voltage and current waveforms with square wave input at resonant frequency [33].

2.6.6 Foreign Object Detection

The FTH pin is a protective feature to prevent unintentional power transmission to foreign objects [33]. The AutoResonant feature, represented by the internal frequency to voltage converter, generates the voltage signal in the LC tank by ensuring resonance coupling (Fig. 2.15). When a foreign conductive object comes into proximity with the TX coil, the effective inductance of the coil is significantly reduced due to the reflected impedance, changing the resonance frequency of the LC tank and thus causing the LTC4125 to adjust its driving frequency to a higher value. This frequency adjustment is detected by the FTH input, which compares the frequency to a preset threshold value. If the frequency exceeds the threshold, the LTC4125 will stop power transmission immediately, preventing potential damage to the foreign object or the system itself. The FTH is programmed with a voltage divider between V_{IN} and ground, according to the following equation 2.15:

$$FTH = \frac{R_{FTH2}}{R_{FTH1} + R_{FTH2}} \cdot 320kHz \tag{2.15}$$

2.6.7 Coil Temperature Threshold

In WPT systems, monitoring the temperature of the TX coil is crucial to avoid overheating and ensure safe operation. The LTC4125 employs an NTC thermistor to monitor the coil's temperature; if it exceeds a certain threshold, it triggers a fault condition. The NTC thermistor used in the LTC4125 of the evaluation kit DC2770A is a MURATA FTN55XH103FD4B thermistor [32]. It has a resistance of $10\,\mathrm{k\Omega}$ (R_{NTC1}) at room temperature (25 °C) and a B factor equal to 3350K. The NTC is placed under the coil as this is the point that suffers the most heating due to parasitic resistance, and in series is placed a resistor (R_{NTC2}) of $10\,\mathrm{k\Omega}$. The NTC hot threshold (V_{NTCH}) is set to 35% of V_{IN}. The fault condition is triggered when the voltage on the NTC (V_{NTC}) falls below V_{NTCH}. This ensures that the coil's temperature remains within safe limits and avoids damage to the device. The resistors R_{NTC1} and R_{NTC2} determine the temperature threshold (T_{HOT}) according to the following equation 2.16:

$$T_{HOT} = \frac{B}{\ln \frac{R_{NTC1}(T_{HOT})}{R_{NTC2}} + \frac{B}{T_0}} \simeq 42°C \tag{2.16}$$

Where T0 is the room temperature in Kelvin (298 K). The T_{HOT} in the LTC4125 in the evaluation kit DC2770A is set to 42 °C to ensure safety. If the coil temperature exceeds this limit, power transmission is interrupted until the coil temperature drops to a safe value.

2.6.8 Algorithm

An algorithm to regulate power transmission precisely was implemented [29, 10]. The CC2640R2F monitors the VCC and VBAT of the LTC4124 every four seconds and sends a message to the TX according to the algorithm. Figure 2.21 show the flowchart of the algorithm. The algorithm dictates that VCC must first surpass the threshold of 3.6 V, as the LTC4124 would trigger a UVCL fault if VCC is less than 3.4 V, and secondly to be greater than VBAT, since it needs to allow the current to flow from VCC to the BAT pin. The algorithm first checks the VCC voltage; if it does not meet the pre-defined threshold of 3.6 V, it sends a message to the TX to increase power. The second check is only performed if the first condition is met and involves evaluating the voltage differential between VCC and VBAT. The VCC should be between 300 mV to 700 mV higher than VBAT. The lower threshold guarantees optimal RX operation and provides a constant charging current, while the upper threshold serves two purposes. First, keeping the VCC below the internal threshold of 1.05 V + VBAT, avoids the activation of the internal switches at the ACIN pin (Fig. 2.6). Secondly, it enables the feedback system to regulate power transmission if the transmitted power is too high, particularly during the final charging phase, when less current is needed, and consequently, less power must be transmitted. The TX's MCU adjusts the voltage output of the DAC, in steps of 2.5 mV, to regulate the transmitted power.

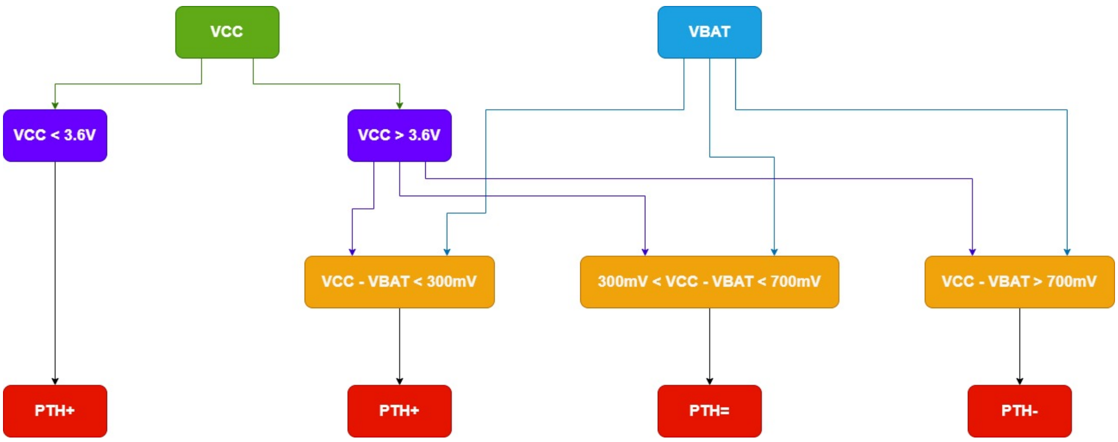

Figure 2.21: Algorithm's flow chart.

Chapter 3

Interventions on the Close-Loop WPT system

The close-loop WPT system developed by Bontempi and Del Bono proved the reliability of the recharging process [29, 10]. However, some improvements can still be performed. One of the system's limitations is that the tests were conducted using a single RX coil with a diameter of 17 mm. As stated previously, the PTE is highly influenced by the size of the RX coil. Therefore, to meet the requirements to develop the WPT system for nDS, it is essential to explore different coils and identify the optimal trade-off between coil size and overall efficiency. Another improvement may be to investigate different receivers rather than only the LTC4124. An RX, like the LTC4126, may be more efficient since, in the evaluation board of the development kit DC2663A-kit, the LTC4126 is provided with a 6 mm coil diameter [34], suggesting a better performance with a smaller coil. Regarding the power management of the device, the buck converter circuit can be improved to ensure the stability of V_{nDS}. Moreover, the algorithm to function properly, relies on the correct measurements of VCC and VBAT taken with the Analog to Digital Converter (ADC) channels of the CCC26040RF. nDS utilize two 16-bit ADC channels to assess the voltages of VBAT and VCC [35]. The ADC's voltage reference matches V_{nDS}. As a result, the voltage range for the ADC spans from 0 V to 3 V. However, both VBAT and VCC have wider voltage ranges. To bring these voltages within the acceptable range, voltage dividers must be employed for VCC and VBAT. Due to these hardware modifications also, firmware interventions are needed to ensure correct computations of the algorithm. Furthermore, to satisfy the requirement of low heat dissipation is fundamental to monitor the RX coil temperature, which can be achieved by implementing an NTC thermistor under the RX coil. In addition, the window selected (VCC - VBAT) for the algorithm can be further reduced to increase PTE. A more efficient system can be achieved by reducing the window, where only the minimum and sufficient power is provided to the RX. This chapter describes the main modifications made to the closed-loop WPT system designed by Bontempi and Del Bono.

3.1 Hardware Interventions

The hardware modifications employed aimed to allow tests using different RX coils, improve the power management of the device, improve the computations of the algorithm, and enable the monitoring of the RX coil temperature. In particular, the following hardware modifications have been performed:

- The PTH circuit has been modified to allow a higher power transmission enabling the testing using different RX coils
- The buck-converter (TPS82740B) circuit was modified for the power management of nDS
- A temperature monitor circuit for the RX coil was developed for tests purposes
- Voltage dividers were introduced for the ADC channels of nDS

3.1.1 PTH Circuit Modification

The objective of finding the best coil, in terms of size and efficiency, implies testing different RX coils guaranteeing the reliability of the charging process. The V_{PTHM} was selected based on an RX coil of 17 mm in diameter. However, this value can be insufficient if a different RX coil is used, above all, if it has a smaller diameter. In Bontempi and Del Bono versions, the maximum value that PTH can achieve, as per equation 2.14, is fixed at almost half of V_{PTHM}, with an additional step of 75 mV when it reaches phase T3 (Fig. 2.18). Therefore, in the case of low coupling (small RX coil), where more power is required from the RX, the TX may not provide a sufficient amount of power to allow the RX to recharge the battery. PTHM, in these terms, sets the upper limit for power transmission. Using the strategy of the charging and discharging of the capacitor, the PTH circuit can vary the V_{PTH} within almost 0 to $\frac{V_{PTHM}}{2}$ + 75 mV. V_{PTH} is not determined by the voltage applied to the PTH pin, but translates in voltage the pulse width of the control signal of the LC tank [33]; for this reason, it cannot be considered an input pin. Due to the modification at the IMON pin, the Optimum Power Search was modified in such a way that the pulse width is limited at the initial pulse width plus one additional step (75 mV). It is possible to control only the initial pulse width, by applying a voltage to the VPTHM pin. Consequently, when the algorithm modifies the threshold (PTH), it must also update PTHM, as failing could result in PTH being stuck at a maximum value, insufficient to allow the RX to recharge the battery. To address this issue, PTHM was connected directly to the second channel of the DAC since it is a real input pin, as shown in figure 3.1, and the relationship 2.14 was used to set the DAC output for PTHM as follows 3.1:

$$PTHM = 2 \cdot PTH + 200mV \tag{3.1}$$

By implementing this modification to the PTH circuit, different RX coils can now be tested, ensuring a reliable recharge process.

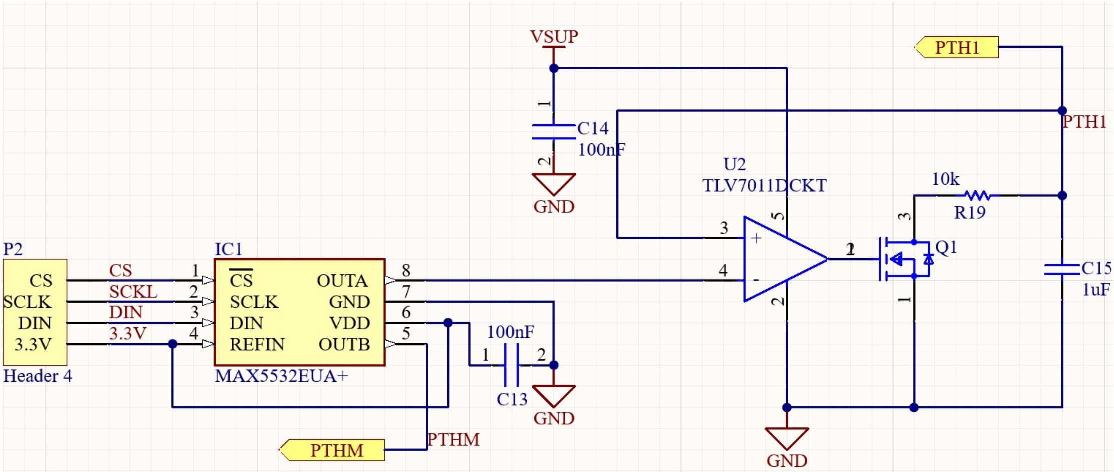

Figure 3.1: PTH modified circuit.

3.1.2 Buck-Converter Circuit

Unlike the LTC4126, where the device has a dedicated pin (OUT pin) for the power supply, the datasheet of the LTC4124 provides a recommendation to connect the power supply to the VCC pin to power a device [30]. However, during the recharge phase, the voltage at the VCC pin is not constant but varies from 3.4 V to approximately 5 V. In the case of nDS, the power supply requires a constant voltage of at least 3 V (V_{nDS}) and an average input current of 5 mA(I_{nDS}) [10, 35]. A buck converter, specifically the TPS82740B, was incorporated between the LTC4124 and nDS to address these requirements. The TPS82740B is optimal for this application for the following reasons [36]:

- The input voltage range is compatible with VCC since it ranges from 2.2 V to 5.5 V
- It can provide an output current up to 200 mA

- It has an efficiency of approximately 95% for an input current like I_{nDS}
- Its output voltage can be hardware programmable to 3 V
- It is sufficiently small with sizes of 2.9 mm x 2.3 mm x 1.1 mm

The buck converter circuit has been modified to ensure stable output and input signals by placing capacitors. As advised by the buck converter's development kit datasheet [37], a 100 µF capacitor has been connected at the input, and a 10 µF capacitor has been placed at the output of the TPS82740B.

3.1.3 Voltage Dividers for the Analog Digital Converter

In the LTC4124, VCC can range from 3.4 V up to 5 V, while VBAT from 2.8 V to 4.2 V. Considering the voltage range for the ADC channels spans from 0 V to 3 V, the voltage dividers to implement need to scale down by a factor of at least 3 V / 5 V. This scaling factor can be approximately achieved by utilizing resistors with values of 39 kΩ and 56 kΩ as stated in equation 3.2.

$$\frac{3V}{5V} \approx \frac{56\,\mathrm{k\Omega}}{56\,\mathrm{k\Omega} + 39\,\mathrm{k\Omega}} \tag{3.2}$$

These values have also been selected because they introduce only an additional current consumption of a few dozen microamperes.

3.1.4 Temperature Monitor Circuit

The European Standard EN45502-1 restricts the surface temperature of an implanted device, stating that it should not exceed 2 °C above the body temperature of 37 °C [38]. Therefore, it is crucial to guarantee that the temperature of the RX coil remains within this prescribed limit. To monitor this temperature during testing, the circuit, shown in figure 3.2, was devised. The circuit makes use of the NTC 103JT-025 and operates on a 5 V power supply. The equation 3.3 establishes the voltage-temperature relationship for accurate temperature measurements.

$$T = \frac{B}{\log \frac{VNTC}{5-VNTC} + \frac{B}{T0+273.15}} - 273.15 \tag{3.3}$$

Where B is a constant at 3452.74, VNTC is the voltage of the NTC, and T0 is 25 °C.

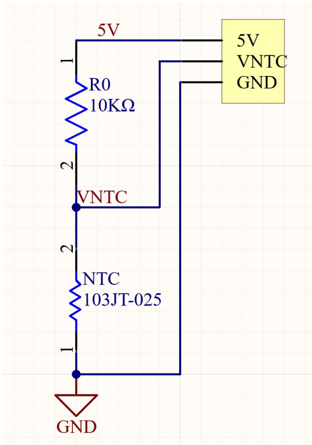

Figure 3.2: Temperature monitor circuit.

3.2 Firmware interventions

3.2.1 Sensor Controller CPU and Signal Filtering

To achieve less power consumption as possible for nDS, the ADC channels are handled not by the main Central Processor Unit (CPU) but by the Sensor Controller CPU, which is a specialized processing unit that operates independently from the main CPU. It is designed to handle sensing and data acquisition tasks while consuming minimal power. By offloading these tasks to the Sensor Controller CPU, the main CPU can remain in a low-power standby mode for extended periods, resulting in significant energy savings. In standby mode, it has a power consumption of only 1.1 µA, while in active mode is the processor current plus 8.2 µA/MHz [35]. To synchronize operations, the system's main CPU wakes up the Sensor Controller every 2 seconds. Once awakened, the Sensor Controller samples each ADC channel every millisecond until 16 samples are taken and it stores the data in a buffer. Once the buffer is complete, the data are sent back to the main CPU, and a median filtering process is applied to eliminate outliers. Filtering the signal is essential for maintaining stability in the algorithm, which relies on the voltage difference between VCC and VBAT. It ensures that the CPU computes the correct values. After filtering, values are converted from bits to millivolts by multiplying them with a scaling factor of 3000/4096. Furthermore, considering that VCC and VBAT were scaled down by a ratio of 56/95, they must be adjusted by the reciprocal of this factor to enable the algorithm to effectively calculate the difference with the correct original values of VCC and VBAT. In Appendix A, the code modifications are presented.

Chapter 4

Tests and Results

This chapter presents the analysis and evaluation of the results obtained from the tests performed. The main goal is to examine the system's performance and characteristics under different conditions, demonstrating its behavior and potential improvements. The tests were categorized into three types, each focusing on a specific investigation. The first type aimed to identify the most suitable receiver for the WPT system. This involved comparing the performance of LTC4126 and LTC4124 receivers using a single MCU (Atmega328p, Arduino) to close the control loop.

The second type aimed to determine the optimal coil in size and efficiency. Table 4.1 summarizes all the coils investigated. The first subgroup tests were performed to characterize each coil, in order to investigate their behavior under various conditions. These conditions included distance variations between the RX coil and TX coil aligned, to understand their impact on system efficiency, lateral misalignments to explore the effects of coil positioning, and angular misalignments to examine the influence of coil orientation on performance. The second subgroup, the recharge tests, involved the two MCUs. The objective of these tests was to recharge the battery completely, emulating the behavior of the implanted device. Consequently, tests involving chicken breasts and physiological saline solution were also conducted. These tests provided insights into the system's performance when integrated with the device and recharging the battery, considering factors such as temperature.

The third type focused on optimizing power delivery by determining the best configuration for the voltage window (VCC - VBAT). Similar to the previous types, this test was performed using a single MCU (Atmega 328p, Arduino). The aim was to identify the settings that maximize power transfer efficiency by systematically varying the voltage window, directly affecting the power delivered to the RX. It's important to note that all tests were made using the LTC4125 with the previously described modifications while maintaining the same TX coil. During the tests, a power supply (RIGOL DP832A) powered the TX. The outcomes of these tests were considered to find the best RX, the best coil in terms of size efficiency trade-off, and the best window to maintain.

Coil	**Diameter (mm)**	**Inductance (µH)**	**Q**
Sunlord, MQQRC060630S8R0	6	8	15
TDK, WR121210-27M8-ID	12	8.32	10
Wurth Electronic, 760308101219	15	11.8	13
Wurth Electronic, 760308101220	17	12.6	20
Wurth Electronic, 760308101214	19	26	30
Wurth Electronic, 760308101104 (TX)	20.5	6.8	42

Table 4.1: Coils Table.

4.1 Test Benches

Two test benches were used to conduct the experiments, each employing a single or dual MCU configuration. In the setup with a single MCU, shown in figure 4.1, the Atmega328p played a dual role as the data reader and controller for both the RX and TX. The power supply was connected in series with a $20\,\Omega$ resistor to simulate the battery. The overall efficiency was computed as per equation 4.1:

$$\eta_{Tot} = \frac{P_{Bat}}{P_{TX}} \tag{4.1}$$

Figure 4.2 illustrates the test bench consisting of two MCUs, which replicated the recharging process and the conditions of the implanted device. The LAUNCHXL-CC2640R2 served as the central TX controller, while the MCU of nDS acted as the peripheral controller for the RX. The RX controller gathers data, such as VCC and VBAT, calculates the difference between them, and transmits a message to the TX based on the algorithm. The message instructs the TX whether to increase, decrease, or maintain the voltage of PTH. The TX, equipped with the DAC and PTH circuit, adjusted the power transmission accordingly. In this configuration, all the previous hardware modifications were applied, and the Arduino was only responsible for saving the data collected by both the RX and TX. Considering the

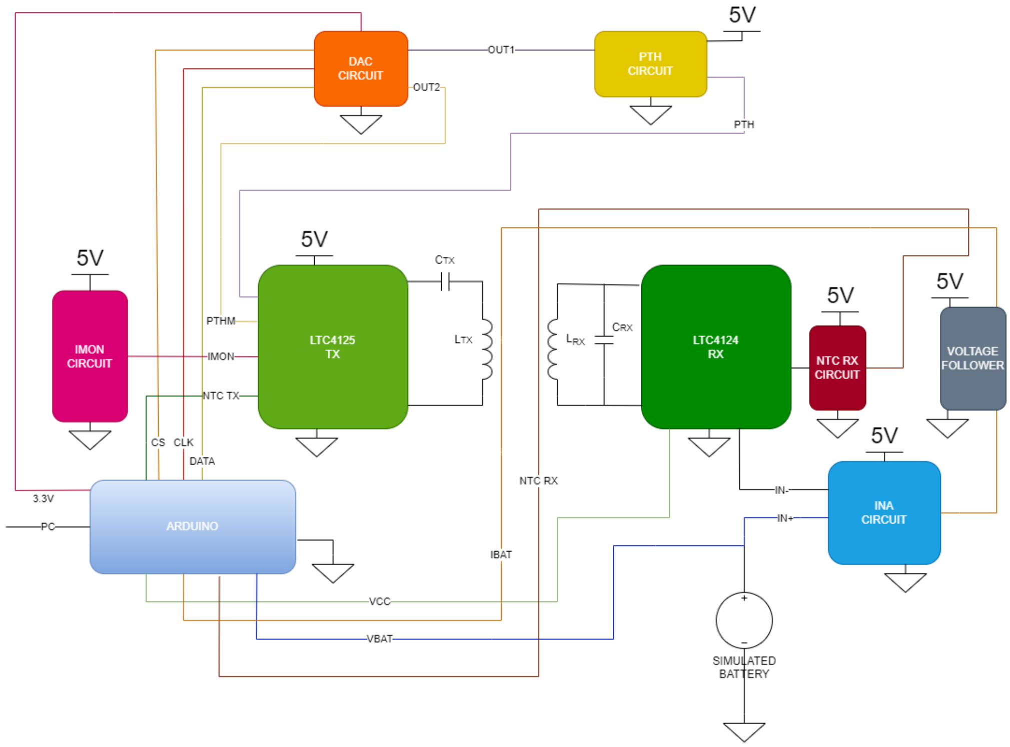

Figure 4.1: Test bench with a single MCU.

buck converter as ideal, since it has an efficiency of 95%, the power required by nDS was computed using the following equation 4.2 :

$$P_{nDS} = VCC \cdot I_{nDS}; \tag{4.2}$$

During the connection mode, I_{nDS} was measured to be in average 5 mA [10]. The overall efficiency was computed as per equation 2.8.

In both test benches, two additional circuits were implemented. One circuit incorporated temperature monitoring of the RX coil, which is crucial to verify that the temperature doesn't rise above the 39 °C. Monitoring its temperature also provides insights into the relationship between coil size and temperature variation. The second circuit monitored the current flowing into the battery, ensuring that the system operated correctly and facilitating the recharging of the battery. This monitoring was achieved by employing a current sense amplifier (INA240) to convert the current into voltage and a voltage follower to maintain the signal's stability. In the first test bench, the Arduino measured and converted the output of the voltage follower to ensure that the current was sufficiently close to the theoretical I_{CHRG}, while in the second test bench, it was used to compute the overall efficiency.

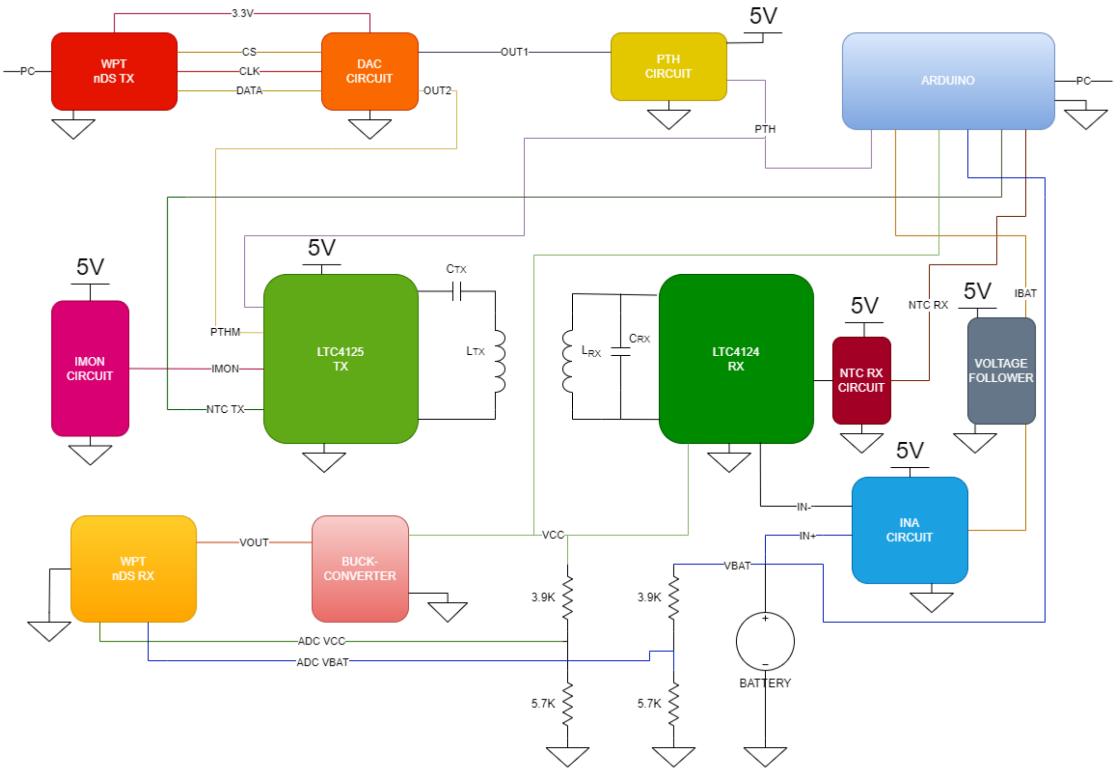

Figure 4.2: Test bench with nDS.

4.2 LTC4124 vs LTC4126

Several tests were conducted to compare the performances of the LTC4124 and the LTC4126. Custom-made boards were created to allow coil switching between the tests, as shown in figure 4.3. The boards were made to replicate the circuit of the respective evaluation board kit [32, 34] with the additional circuit for temperature RX coil monitoring. The test bench used is the one with a single MCU. The experiments used two coils: the 6 mm coil and the 19 mm coil, reported in table 4.1. The 6 mm coil was chosen because it came with the evaluation board of the LTC4126 in the DC2663A-KIT [34], suggesting an optimal performance with coils with few milliliters of diameter. The 19 mm coil, on the other hand, was selected due to its larger size, allowing it to achieve a higher coupling coefficient. Each test was performed by varying the distance between the RX and TX from 1 mm to 20 mm, with an increment of 1 mm. Additionally, the selected V_{CHRG} was at 4.2 V. The VBAT was varied from 2.8 V to 4.1 V, with a step size of 0.1 V. The window voltage (VCC - VBAT) used by the algorithm was between 200 mV and 250 mV. For each coil and at each step, the power supplied to the TX (P_{TX}) by the RIGOL DP832A was read, and the overall efficiency was calculated using equation 2.8.

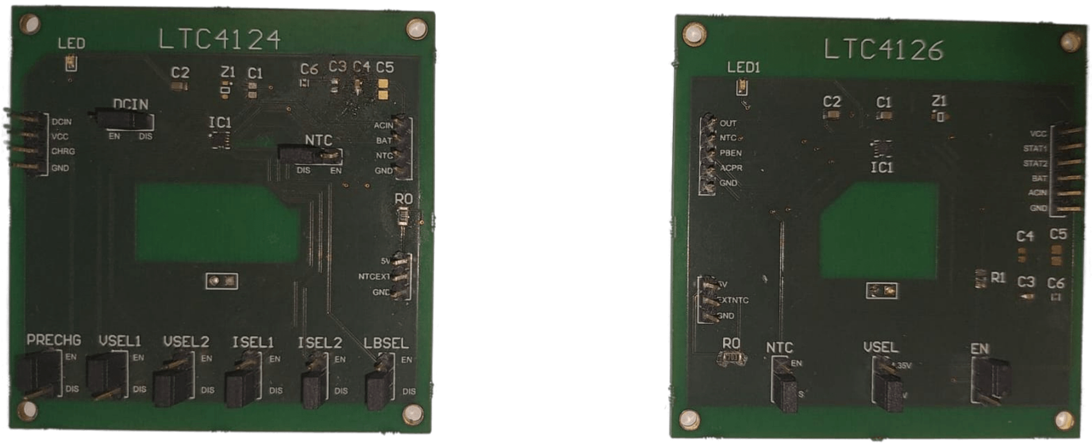

Figure 4.3: LTC4124 and LTC4126 custom-made boards.

The comparison between the LTC4124 and the LTC4126 revealed distinct differences in their performance as wireless battery chargers. As shown in figure 4.4, the LTC4126 utilizing the 6 mm coil achieved a peak efficiency of approximately 6% at a distance of 2 mm. In figure 4.5, the LTC4124 reached a significantly higher peak efficiency of 18% at the same distance. The LTC4126 and the LTC4124 experienced a loss of power beyond 9 mm of distance with the 6 mm coil. The interrupting of power transmission is due to a higher request of power by the RX that overheats the TX coil above the programmed threshold of 41 °C. This event triggers the fault condition of the temperature fault, which forces the Optimum Power Search algorithm of the LTC4125 to restart. As reported in figure 4.6 and in figure 4.7, the LTC4126 with the 19 mm coil attained its maximum efficiency of 8% at a distance of 4 mm. In comparison, the LTC4124 exhibited a remarkably higher peak efficiency of 35% at 7 mm of distance. In this condition, the LTC4126 ceased to receive power at 12 mm, whereas the LTC4124 reached its limit at 20 mm.

Several factors contribute to the superior performance of the LTC4124 as a wireless power receiver. Firstly, the LTC4126 incorporates an additional feature, the step-down DC/DC converter, to power hearing aid ASIC. However, this converter necessitates additional power, thus reducing the overall efficiency of the LTC4126. Secondly, the LTC4126 delivers a lower current of 7.5 mA to the battery, whereas the LTC4124 supplies a higher current of 10 mA. This discrepancy in current has a direct impact on the overall efficiency, as the computation of P_{Bat} has been made considering the theoretical I_{CHRG} provided by the datasheets [31, 30]. Therefore, a lower current translates to a lower power absorbed and, subsequently, to a reduction in the overall efficiency computation (eq. 2.8).

Considering these factors, the LTC4124 demonstrated itself as a better choice for implementing the WPT system in nDS. It achieved higher efficiencies due to the absence of the additional power request of the DC/DC converter and thanks to a higher I_{CHRG}.

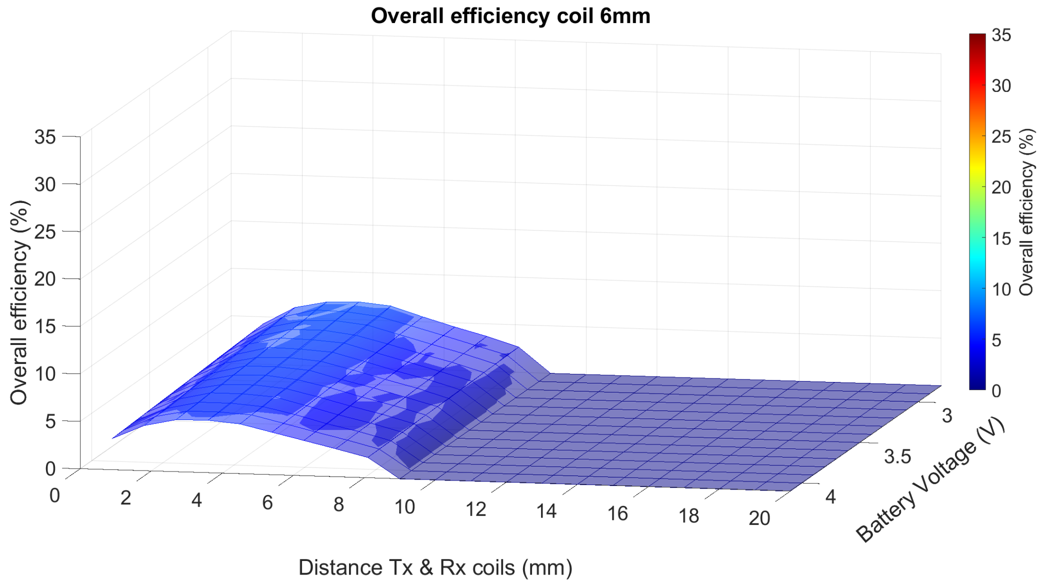

Figure 4.4: Overall efficiency LTC4126 with coil 6 mm.

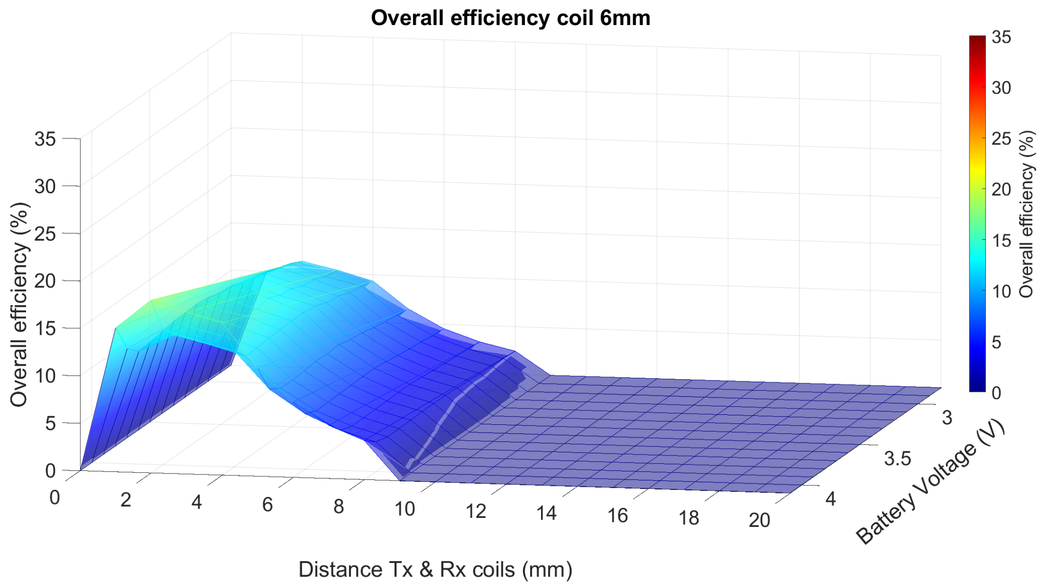

Figure 4.5: Overall efficiency LTC4124 with coil 6 mm.

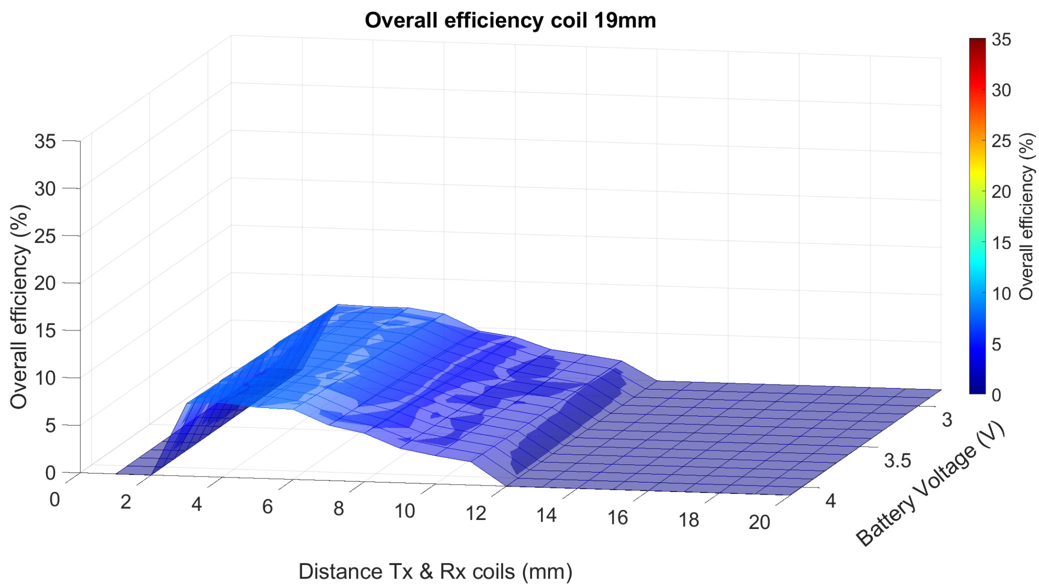

Figure 4.6: Overall efficiency LTC4126 with coil 19 mm.

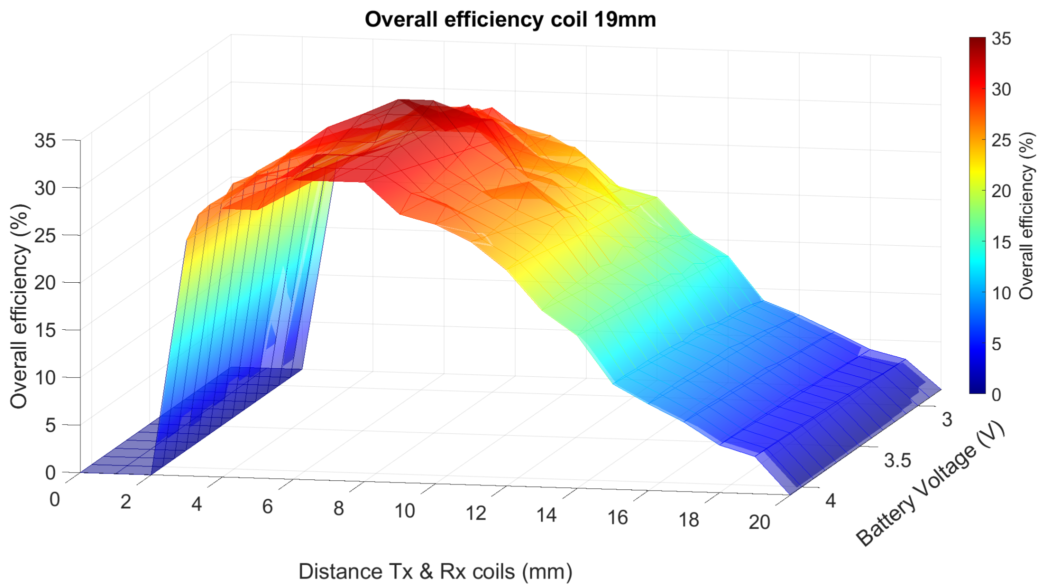

Figure 4.7: Overall efficiency LTC4124 with coil 19 mm.

4.3 Characterization Tests with Simulated Battery

Once selected the LCT4124 as best RX, it is essential to characterize each coil under different conditions to find the best RX coil for the implementation in the WPT system. This characterization involves conducting tests using the test bench equipped with a single MCU. Since the PTE of a WPT system relies heavily on the relative positions and sizes of the coils, as stated in equation 2.3 [26], three typologies of tests were performed for each coil. The objective of these tests was to assess the behavior of each coil when subjected to three different variations in spatial disposition:

- Distance variation with the coils aligned
- Lateral displacement at a fixed distance
- Angular displacement at a fixed distance

To assess the behavior of the coils under distance variation with the coils aligned, measurements of the power supplied to the TX (P_{TX}) were taken with the distance between RX and TX coils ranging from 1 mm to 20 mm, with increments of 1 mm. As shown in figure 4.8, for the lateral displacement tests, the coils were laterally displaced from 0 mm to 8 mm, with increments of 1 mm, while maintaining a fixed distance. Similarly, for the angular displacement tests, the coils were displaced from 0° to 12°, with increments of 2°, while keeping the distance fixed. A fixed distance of 6.5 mm (±0.5 mm) was selected for all measurements. Assuming the I_{CHRG} to be 10 mA and the selected V_{CHRG} to be 4.2 V, the overall efficiency was then calculated using equation 2.8 In addition taking into account skin thickness to be between 1 mm to 4 mm [39], encapsulation of future RX board, and future TX housing a distance range of 6.5 mm (±0.5 mm) was considered as a standard performance metric for this WPT system. In all tests, the battery voltage varied from 2.8 V to 4.1 V with increments of 0.1 V, and the window voltage (VCC - VBAT) used by the algorithm was selected to be between 200 mV and 250 mV.

4.3.1 Distance Variations

The results of the coil characterization tests concerning the distance variation with the coils aligned are presented in figure 4.9, 4.10, 4.11 and 4.12. Analysis of the distance variations tests using the 6mm coil (Fig. 4.9) indicated that the highest distance achieved was 9 mm. Beyond this distance, the TX triggered the temperature fault exit condition interrupting the power transmission. The 6 mm coil showed a peak efficiency of about 13% at a distance of 2 mm. On the other

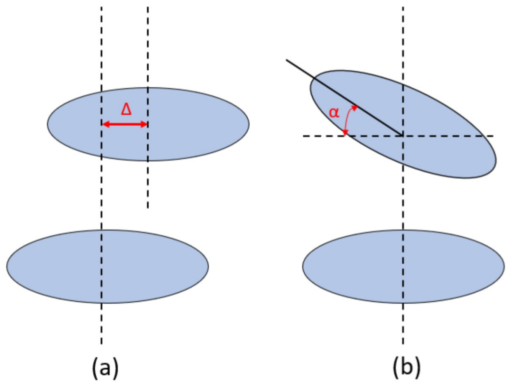

Figure 4.8: a) Lateral displacement configuration b)Angular displacement configuration [29].

hand, the 12 mm coil (Fig. 4.10) reached a maximum distance of 11 mm, before encountering similar problems. At 5 mm of distance, it showed a peak efficiency of 9%. Despite the 12 mm coil's average efficiency was lower than the 6 mm coil due to a lower quality factor, the 12 mm coil demonstrated more robustness achieving a higher distance due to its larger diameter. The 15 mm coil achieved a maximum distance of 16 mm and a peak efficiency of approximately 20% at 8 mm (Fig. 4.11). The 19 mm coil attained a maximum distance of 19 mm, before encountering a fault condition (Fig. 4.12), reaching a peak efficiency of 35% at a distance of 7 mm. The reported efficiencies at the distance of 6.5 mm were 5%, 8.5%, 19.5%, and 31% for the 6 mm, 12 mm, 15 mm, and 19 mm coils, respectively.

Contrary to expectations, where smaller distances imply a higher coupling coefficient and thus higher efficiency [26], it can be noted that for distances lower than 4 mm, each coil exhibited lower efficiencies. The LTC4125 has an integrated resonance frequency tuning system [33], and it has been observed that, for very low distances, the resonance frequency ranges from 200 kHz to 300 kHz. A lower distance amplifies the impact of the reflected impedance on the TX LC tank. Thus, the AutoResonant feature increases the driving frequency to achieve the resonant coupling. For example, the 19 mm coil at 1 mm of distance exceeded the FTH triggering the Foreign Object Detection fault condition of the LTC4125 and interrupting the power transmission. By multiplying each term of the equation 2.12 by f_n, it can be proved that the duty cycle of the control signal of the LC tank increases with the resonance frequency (eq. 4.3).

$$DC = (0.24 \cdot V_{PTH}) + 150ns \cdot f_n; \tag{4.3}$$

It can be concluded that raising the resonance frequency, as a consequence of shorter distances between the coils, results in higher power transmitted than expected, leading to reduced efficiency.

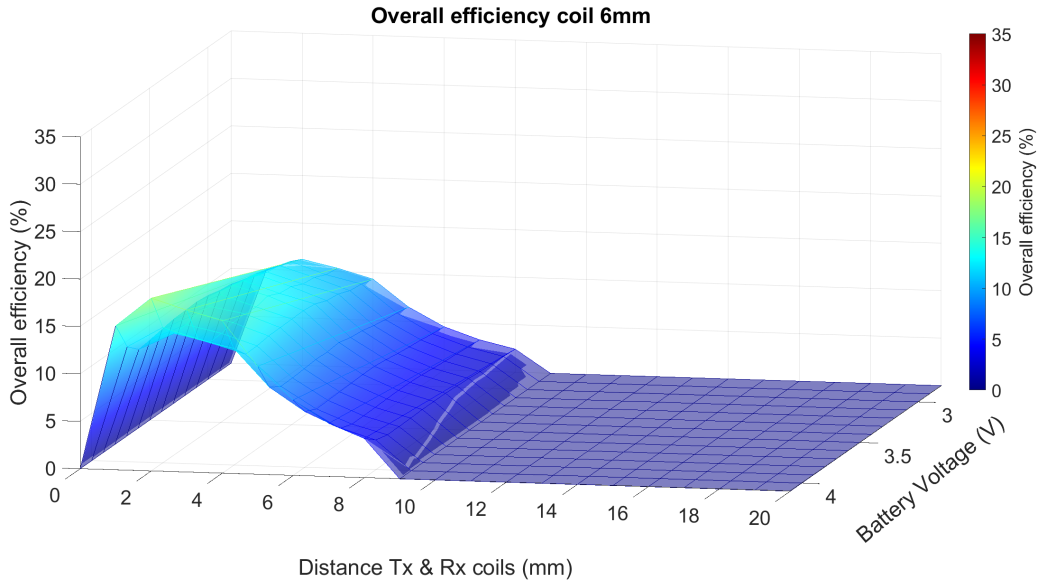

Figure 4.9: Overall efficiency coil 6 mm.

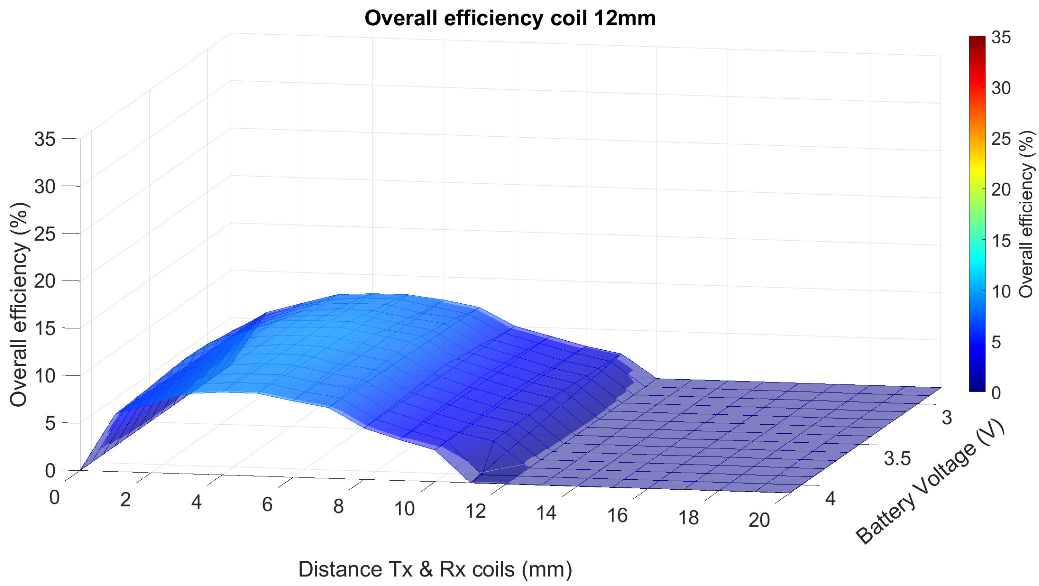

Figure 4.10: Overall efficiency coil 12 mm.

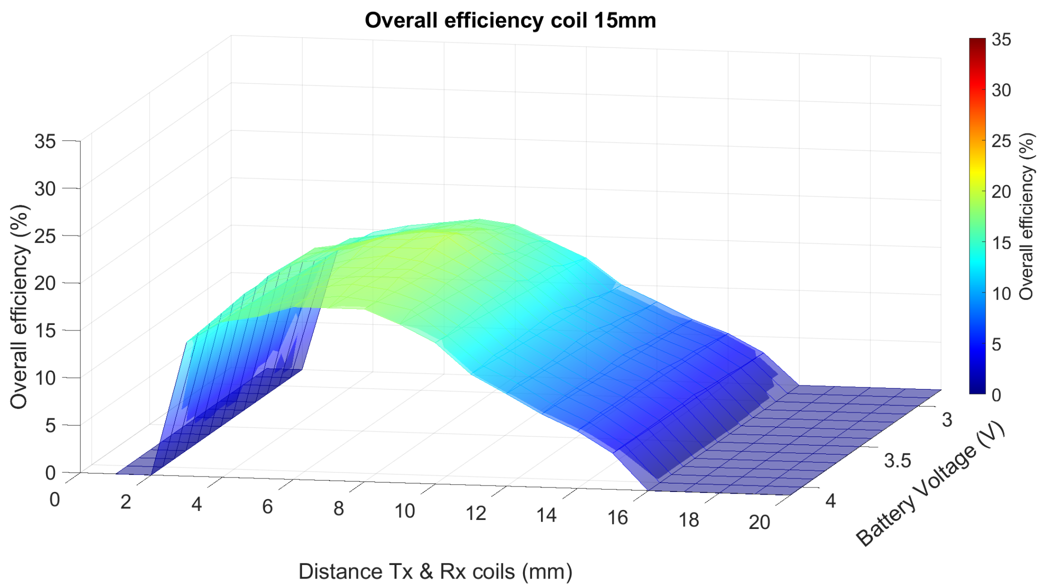

Figure 4.11: Overall efficiency coil 15 mm.

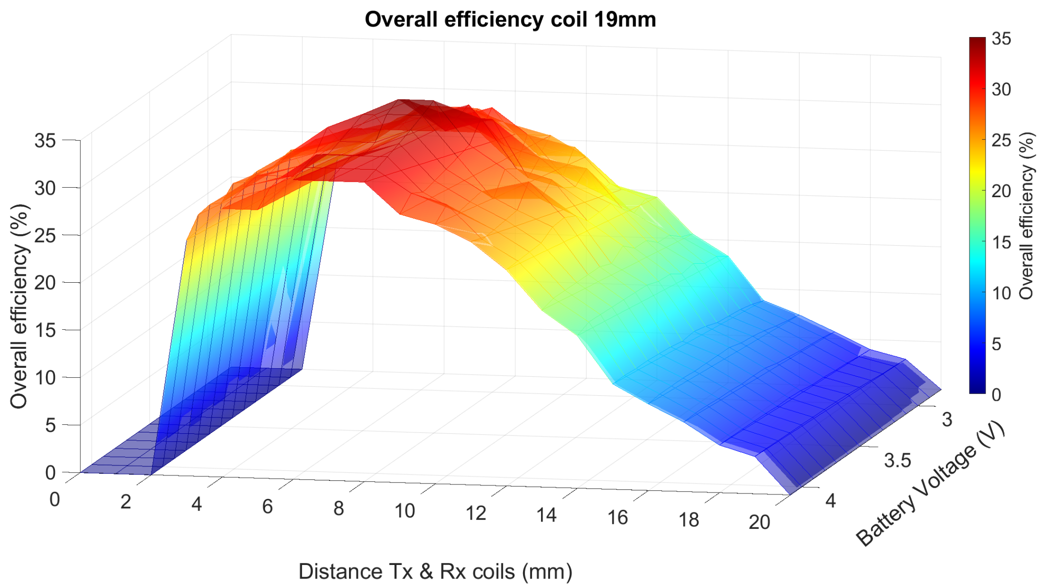

Figure 4.12: Overall efficiency coil 19 mm.

4.3.2 Lateral Misalignments

Figures 4.13, 4.14, 4.15 and 4.16 illustrate the results of the lateral misalignments characterization test. The 6 mm coil (Fig. 4.13) showed a relatively stable efficiency of approximately 5% until a displacement of 5 mm, after which the power requested exceeded the TX capacity, triggering temperature fault condition. The 12 mm coil (Fig. 4.14) achieved a higher efficiency of 8% until 6 mm before experiencing a significant decline, with an efficiency drop to about 4% at the maximum tested displacement of 8 mm. The 15 mm coil (Fig. 4.15) exhibited an efficiency of 18% until 6 mm before experiencing a drop, and at 8 mm, its efficiency reached approximately 10%. The 19 mm coil (Fig. 4.16) showed the best performance among all tested coils exhibiting an efficiency of 30% until 6 mm before experiencing a decline, and at 8 mm, it achieved an efficiency around 17%. Only the 6 mm coil experienced an interruption in power transmission before reaching the 8 mm mark. These results indicate that a coil with a larger diameter is more reliable because it can absorb a higher quantity of magnetic flux generated by the TX [26], which results in more robustness and higher efficiencies over lateral misalignments.

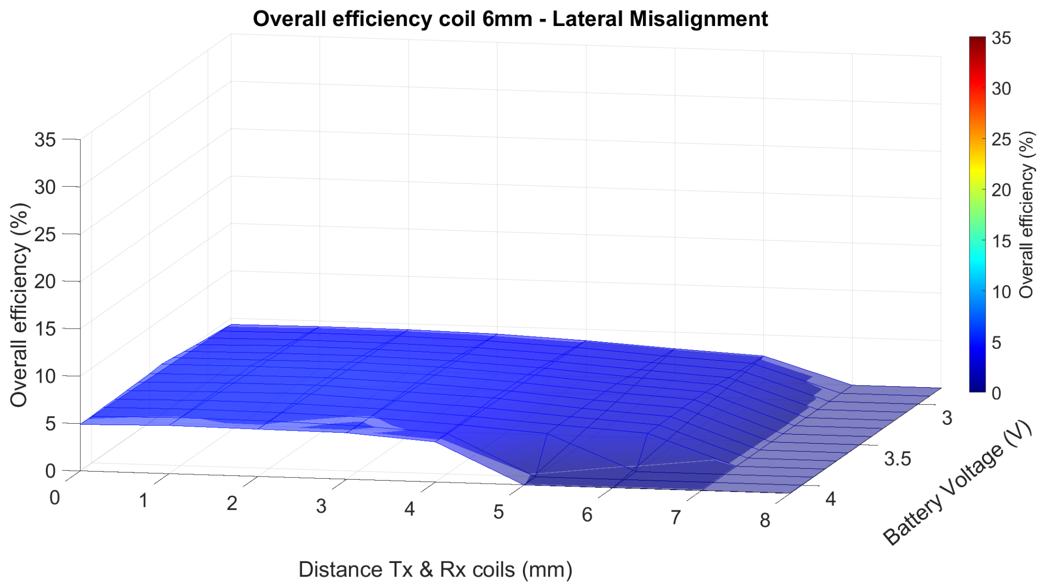

Figure 4.13: Overall efficiency coil 6 mm Lateral Misalignment.

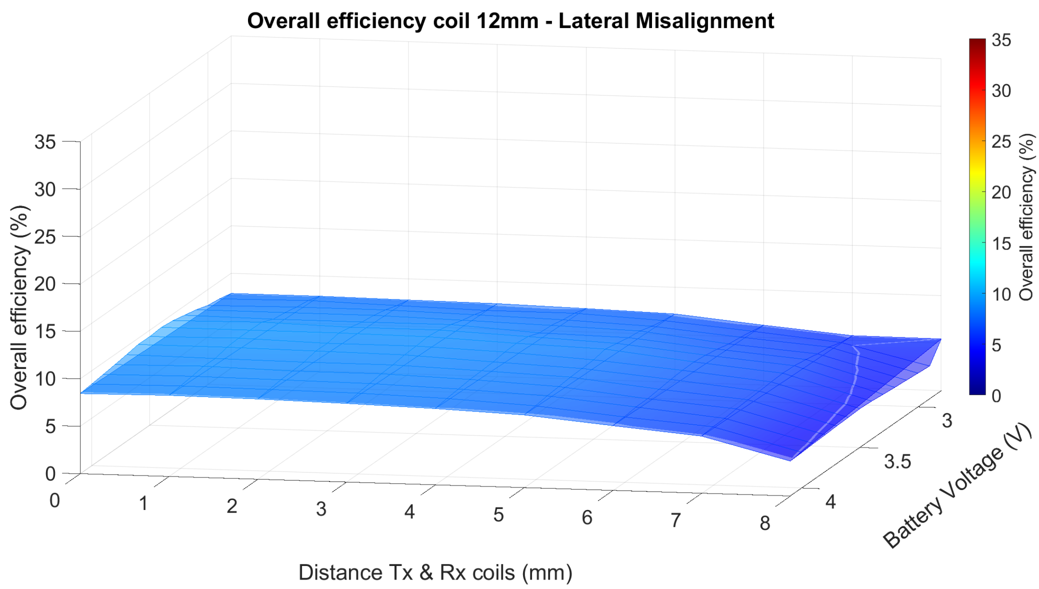

Figure 4.14: Overall efficiency coil 12 mm Lateral Misalignment.

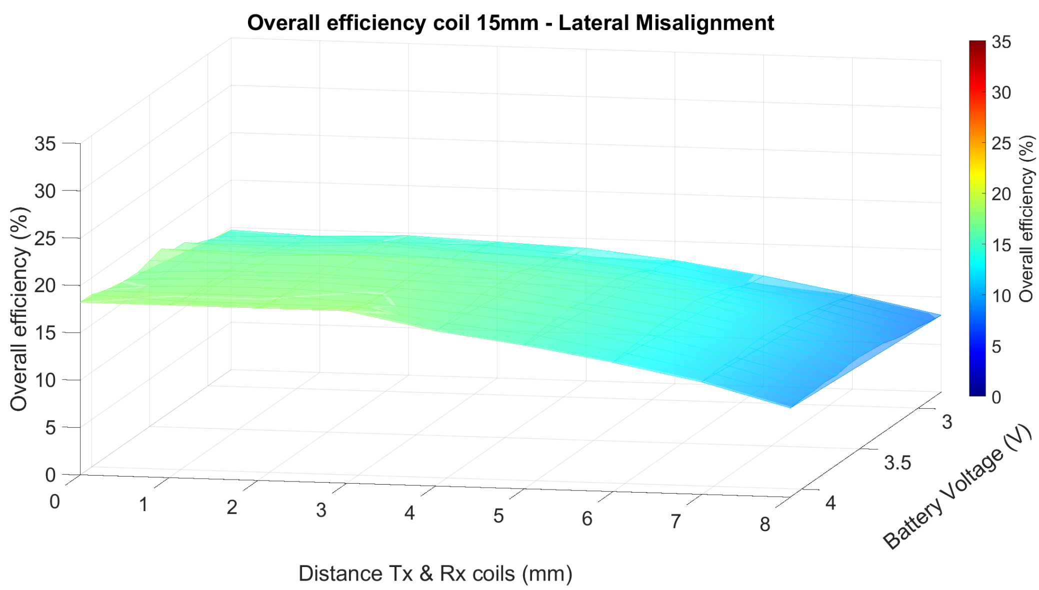

Figure 4.15: Overall efficiency coil 15 mm Lateral Misalignment.

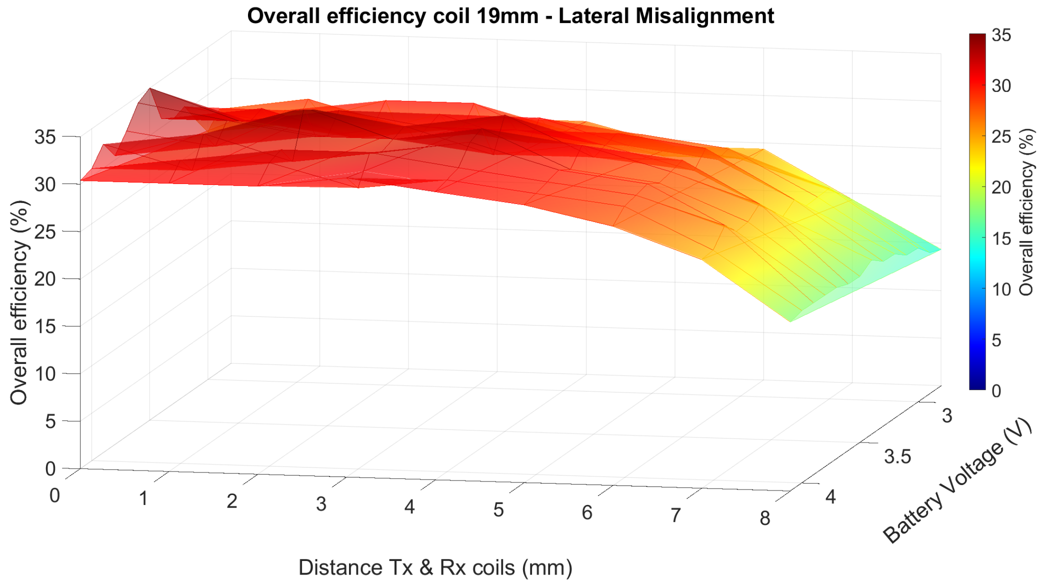

Figure 4.16: Overall efficiency coil 19 mm Lateral Misalignment.

4.3.3 Angular Misalignments

The results of the angular misalignment characterization tests are presented in figures 4.17, 4.18, 4.19 and 4.20. The 6 mm coil (Fig. 4.17) showed a decline in efficiency at 2°, and due to the high power request, the LTC4125 encountered in the temperature fault condition at 4°. The 12 mm coil (Fig. 4.18) maintained an efficiency of 8% until 4° before showing a significant loss. The power transmission stopped at 10° due to the same issues as the 6 mm coil. The 15 mm coil (Fig. 4.19) demonstrated an efficiency above 15% until 4°, after which it began to drop. At the maximum tested angular displacement of 12°, its efficiency decreased to approximately 6%. The 19 mm coil (Fig. 4.20) maintained an efficiency of around 30% before it began to decrease at 10° and at maximum tested angular displacement, its efficiency had fallen to 23%. Only the 6 mm and 12 mm coils experienced shutdowns before the 12° mark. These results indicate that a coil with a larger diameter is more reliable and efficient, for the same reasons discussed for the lateral misalignments results.

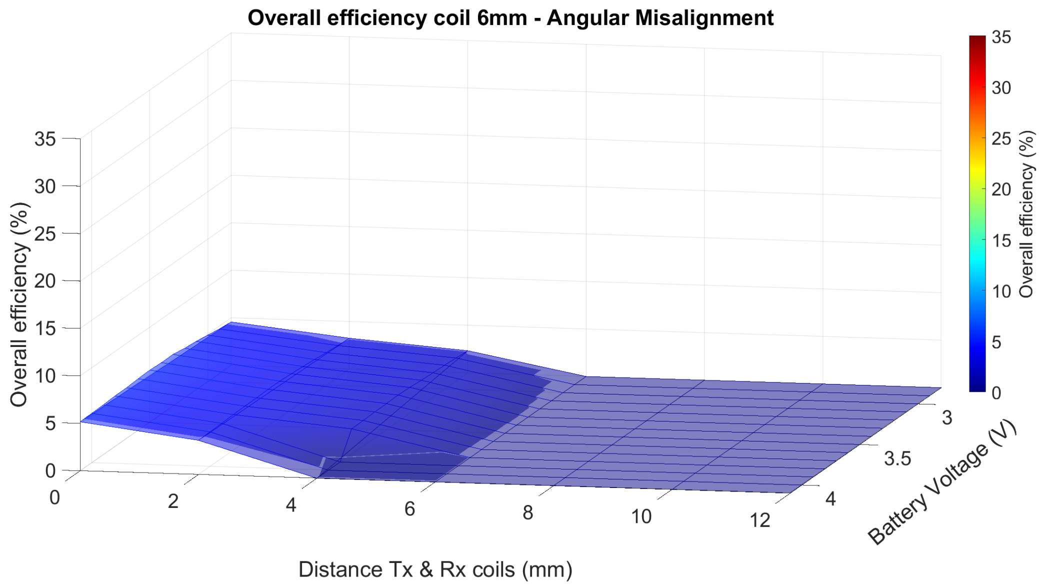

Figure 4.17: Overall efficiency coil 6 mm Angular Misalignment.

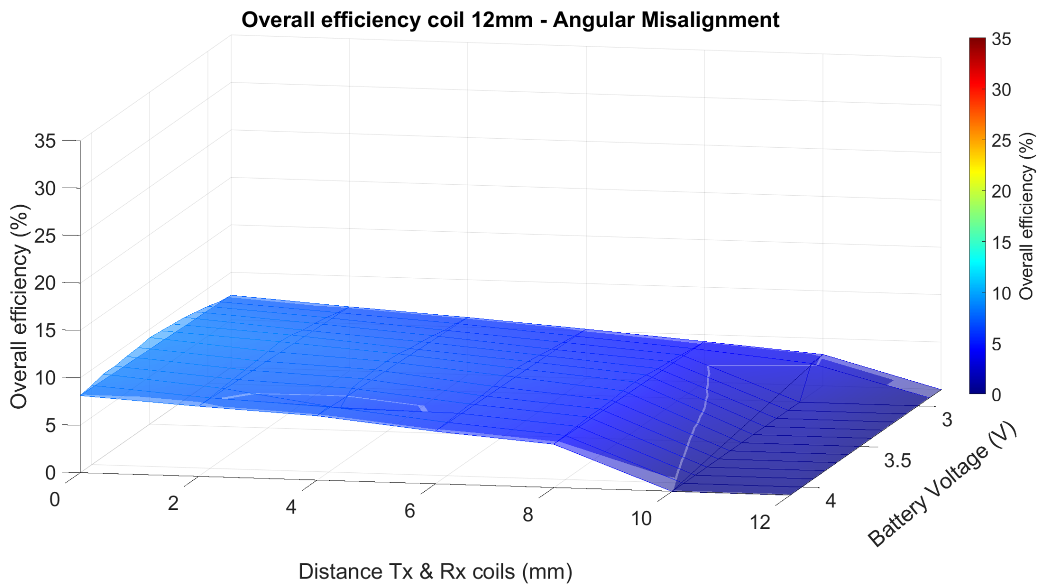

Figure 4.18: Overall efficiency coil 12 mm Angular Misalignment.

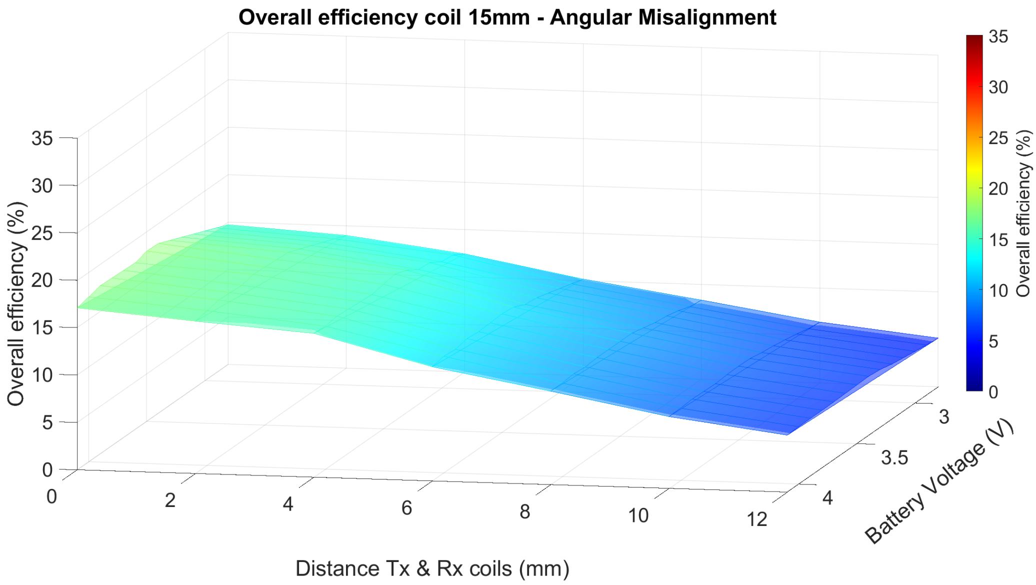

Figure 4.19: Overall efficiency coil 15 mm Angular Misalignment.

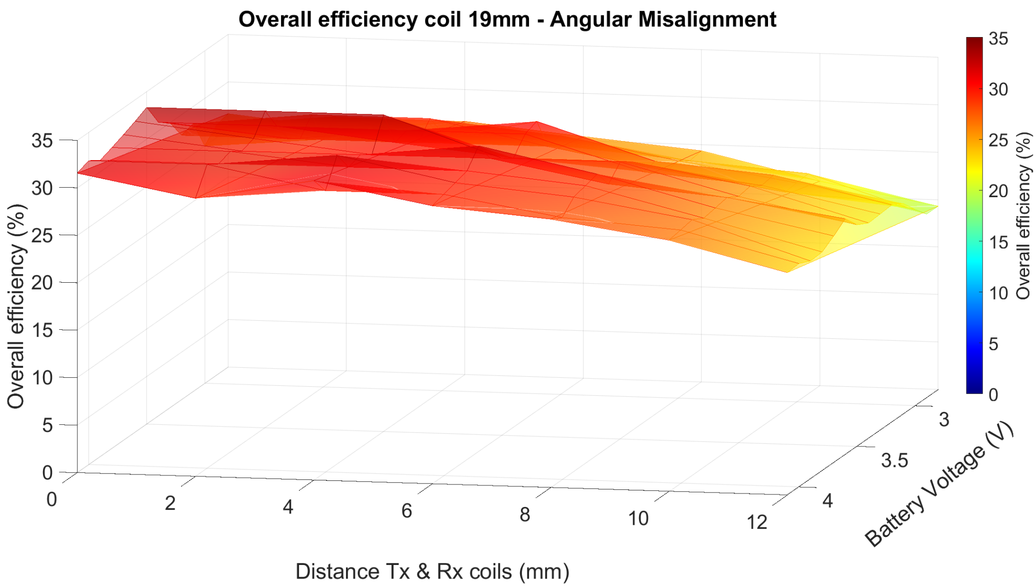

Figure 4.20: Overall efficiency coil 19 mm Angular Misalignment.

4.4 Characterization Tests with Battery

After characterizing each coil in different spatial, the objective is to identify the best coil that exhibits the highest efficiency and the lowest temperature variation in a complete battery recharge. To accomplish this, the test bench equipped with 2 MCUs was utilized. The testing procedure consisted of a complete battery recharge, which took approximately 200 minutes. The LIR2025 battery was selected based on its optimal balance between capacity, charging time, overheating, recharge duration, and physical dimensions [10]. P_{TX} measurements were taken every 15 minutes by reading the power from the power supply. Table 4.2 presents the results obtained from the uninterrupted monitoring of recharge tests conducted using the BLE communication, with air as the intermediary medium. The window voltage (VCC - VBAT) used by the algorithm was selected to be between 300 mV and 700 mV. Each coil was tested at distances between RX and TX coil of 2.5 mm and 6.5 mm to simulate the minimum and maximum possible skin thickness [39]. For both distances, it's reported the power required by the TX and the RX, the average and maximum efficiency, the maximum value of PTH, and the maximum temperature variation on the TX and RX coil, which have been referred to an initial room temperature of approximately of 25 °C.

Coil (mm)	d (mm)	PTX_{max} (mW)	PL_{max} (mW)	η_{avg} (%)	η_{max} (%)	PTH_{max} (mV)	ΔT_{TX} (C°)	ΔT_{RX} (C°)
12	2.5	704	52	5.8	8.1	599	16.3	36.1
12	6.5	604	52	7.6	9.5	534	9.5	21.2
15	2.5	395	48	11.4	13.6	653	7	11.6
15	6.5	295	47	13.1	16.5	466	3.5	8.8
17	2.5	355	48	11	14	715	6.6	9.6
17	6.5	250	48	13.3	19.3	367	4	5.6
19	2.5	220	52	21.1	24.3	292	3.5	4.9
19	6.5	180	56	26.3	32.3	251	1.4	1.7

Table 4.2: Recharge Test Table.

Relying solely on the peak efficiency is insufficient for evaluating the system's quality in applications where robustness and reliability are crucial under various conditions. Despite the 6 mm coil showed a higher peak efficiency compared to the 12 mm coil, it demonstrated very low robustness in the displacements test. Due to its inability to withstand real-life challenges, such as misalignments possibly caused by animal movements in an in-vivo experiment, it was not able to proceed to the recharge test phase. Instead, the 17 mm coil was included since it was already characterized and demonstrated a good performance [29]. The data demonstrate that smaller RX coils, with respect to larger RX coils, result in lower efficiency and higher temperatures for both the TX and RX coils. The RX and TX coils overheat because of the Joule effect, where the electric current encounters resistance within the coil, converting electrical energy into heat. This heating effect is caused by the inherent resistance of the wire used in the coil and can be intensified by high current or excessive voltage. The TX coil overheats because it delivers more power to satisfy the smaller RX coil's increased power demand. On the other hand, the RX coil overheats because it receives more power, resulting in greater power dissipation through the Joule effect. Considering this perspective, the data reveals that the 12 mm coil performs poorly than the other tested coils. It achieves maximum efficiency of only 8% and exhibits a significant temperature variation of 36 °C. In contrast, the 19 mm coil is the best performer, with a maximum efficiency of 32% and a minimal temperature variation of 1.7 °C. This highlights the substantial impact of the RX coil size on the WPT systems. As for the characterization tests, the results show that for the same coil, efficiencies at 2.5 mm are lower than ones at 6.5 mm; this is due to the AutoResonant feature of the LTC4125, which increases the f_n at lower distances resulting in excessive power transmission. No tests exhibited interruption of the recharge process proving the reliability of the new modified WPT system. In addition to the tests with air as an intermediary medium, experiments were carried out using animal tissue, specifically chicken breast, and saline solution as an intermediary medium to simulate the recharging process in an in-vivo environment. These experiments focused on the 12 mm coil at 2.5 mm of distance as it exhibited the highest level of overheating. By examining its performance, we can gain valuable insights into the system, particularly regarding how much heat the intermediary medium can dissipate under the worst conditions. Table 4.3 reveals that introducing tissue as an intermediate medium does not significantly decline efficiency. However, the tissue interposition aids in regulating the temperature rise due to its water content and leading to a lower temperature RX coil variation of 18.7 °C. Furthermore, the test with the saline solution, achieving a temperature RX variation of 9.3 °C, reinforces the notion that the mediums with high water content help manage temperature elevation. Consequently, the tissue's ability to mitigate overheating is anticipated to be further enhanced in environments characterized by blood perfusion [40].

Interposed medium	PTX_{max} (mW)	PL_{max} (mW)	η_{avg} (%)	η_{max} (%)	PTH_{max} (mV)	ΔT_{TX} (C°)	ΔT_{RX} (C°)
Air	704	52	5.8	8.1	599	16.3	36.1
Animal tissue	505	46	6.6	9.7	523	14.8	18.7
Saline solution	604	51	6.6	9.5	571	5.3	9.3

Table 4.3: Recharge In Vivo Simulated Test Table.

Based on the requirements and the results, several criteria have emerged as essential factors in evaluating the optimal coil. These criteria include size, efficiency, robustness, and temperature. Table 4.4 summarizes the evaluation results for each coil based on these parameters. The 19 mm coil is the most favorable choice among the coils tested, proving the highest efficiencies, best robustness, and lowest temperature variation. Despite its larger size, it can still be integrated into the future device.

Coil(mm)	**Size**	**Efficiency**	**Robustness**	**Temperature**
6	++	-	-	/
12	++	-	+	-
15	+	+	+	+
17	+	+	++	++
19	+	++	++	++

Table 4.4: Table Comparison.
Symbols used and meaning: (-) bad, (+) good, (++) very good.

4.5 Window Test

The power delivered to the RX in the system depends on the PTH signal, as it controls the pulse width of the control signal of the LTC4125 LC tank, and thus the power delivered [33]. A higher PTH signal corresponds to a higher amplitude in the RX LC tank (ACIN pin) and thus a higher VCC [30]. Thanks to the control loop, the power requested by the RX can be controlled by modifying the window size, thereby regulating the amount of power delivered to the system. This control is essential for optimizing the overall system efficiency.

The test was conducted using a single MCU. The RX coil was the 19 mm coil positioned at the fixed distance of 6.5 mm from the TX coil. The simulated VBAT was set at 3.6 V, and a window size of 20 mV was chosen to determine the difference between VCC and VBAT. Figure 4.21 illustrates the results obtained, displaying on the x-axis only the lower bound of the window size for each sample. For instance, the first sample indicates the range from 100 mV to 120 mV, and so on. The decision to limit the test range to 300 mV, rather than the upper bound of 700 mV used by Bontempi and Del Bono [29, 10], was based on the fact that the lower bound determines the minimum power transfer and during the recharge the difference would mostly be around it. Additionally, the upper bound only needs to be below the threshold of the LTC4124 comparator, which is 1.2 V.

The results indicate that the TX failed to transmit sufficient power when the difference was below 100 mV. The maximum efficiency was achieved at 120 mV. Beyond that point, efficiency gradually decreased. There was an overall efficiency loss of 5% from the peak efficiency until the last sample. Considering the need for a sufficiently higher window from the 100 mV threshold to maintain system functionality and the requirement of a reasonably large window to prevent too frequent PTH changes, a window size of 200 mV - 250 mV was considered optimal.

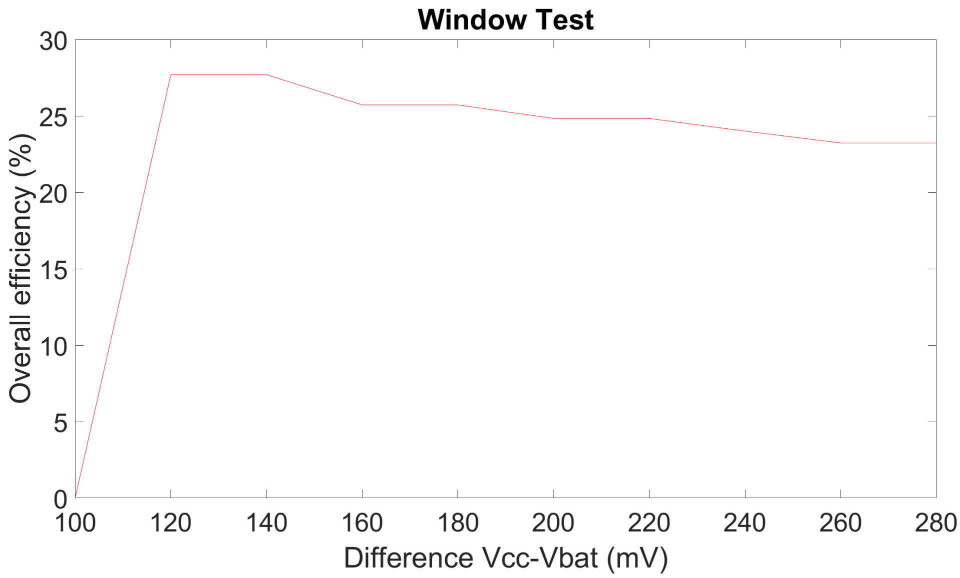

Figure 4.21: Window Test.

A recharge test with the 19 mm coil at 6.5 mm of distance was performed with the new selected window. Table 4.5 reports the results compared to the previous test with a voltage window of 300 mV - 700 mV. The results indicate a deterioration in system performance, reaching an average efficiency of 18.4% compared to the 26% achieved in the previous test. However, these deteriorations are due to the measurement components' non-ideal nature and to no perfect reproducibility of the results. The Arduino does not always measure the current accurately, as shown in figures 4.22, 4.23, and it is not always possible to position the RX and TX coils exactly 6.5 mm distance between them. In the previous test, the measured current was slightly higher, resulting in a higher battery power consumption and higher efficiency. In addition, as expected, the lower VCC achieved in the test with the new window decreases the value of P_{nDS} made by computation considering the buck-converter ideal(eq. 4.2). However, these refinements can be considered second-order compared to the coil's choice and the window's optimization.

Window (mV)	d (mm)	PTX_{max} (mW)	PL_{max} (mW)	η_{avg} (%)	η_{max} (%)	PTH_{max} (mV)	ΔT_{TX} (C°)	ΔT_{RX} (C°)
300-700	6.5	180	56	26.3	32.3	251	1.4	1.7
200-250	6.5	195	44	18.4	24.8	271	2	1.6

Table 4.5: Old Window and New Window Recharge Test Table.

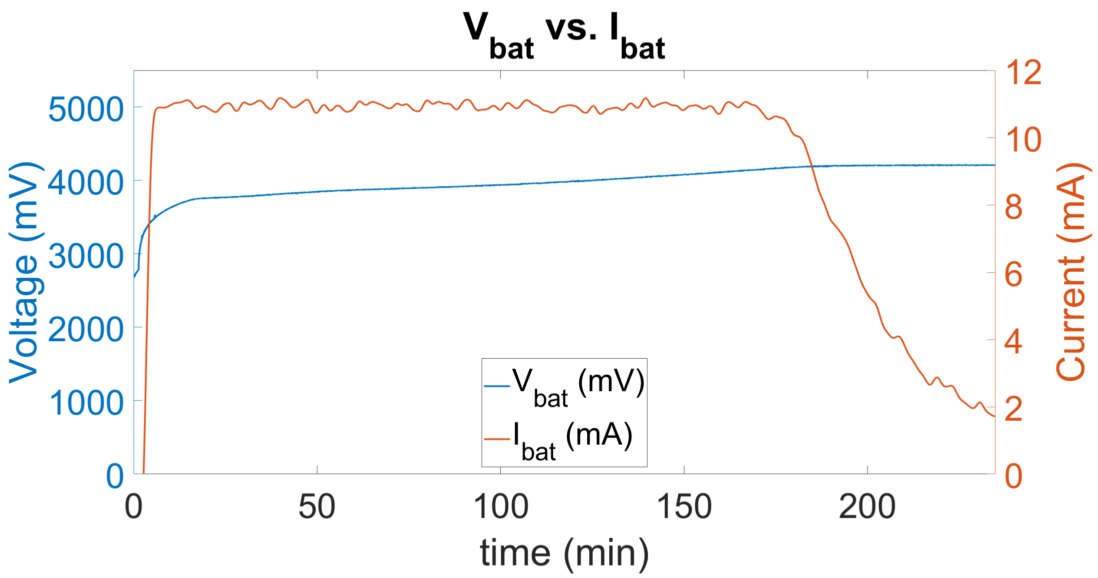

Figure 4.22: Battery charging profile with a window of 300 mV - 700 mV.

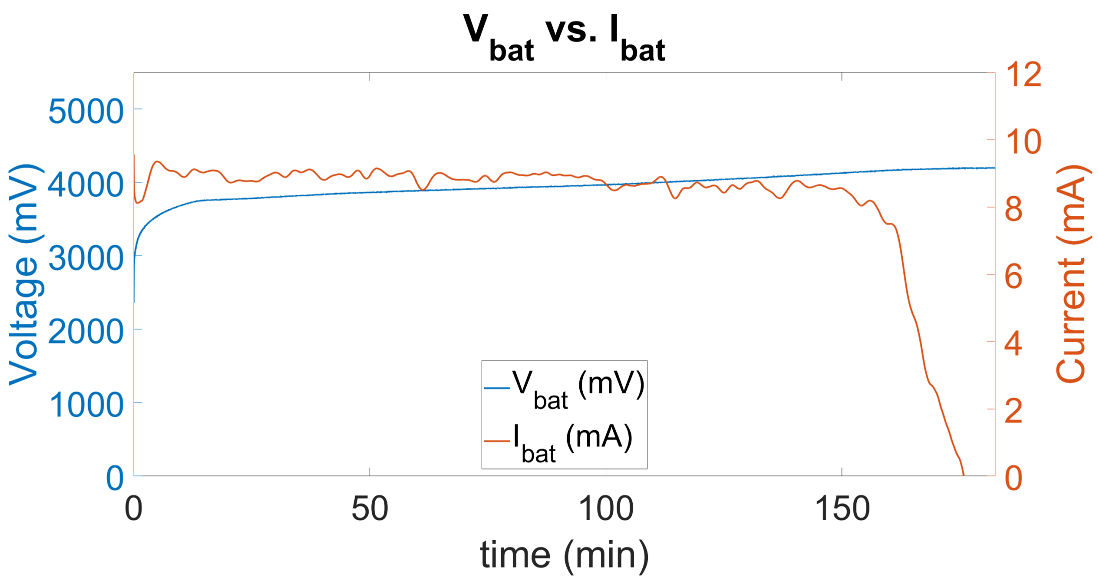

Figure 4.23: Battery charging profile with a window of 200 mV - 250 mV.

4.6 Optimization Closed-Loop WPT system

From the evaluation of the results, it emerged that the LTC4124 is the best RX, and the 19 mm coil is the best RX coil. The LTC4124 demonstrated better performance compared to the LTC4126, and the 19 mm coil showed higher efficiencies than all other coils with temperature variation within the acceptable standards [38]. In conclusion, the WPT system developed for nDS is based on the closed-loop WPT of Bontempi and Del Bono with the following interventions:

- Transmitter LTC4125
  - Modification at the PTH circuit allowing to transmit more power.
- Receiver LTC4124
  - 19 mm coil as RX coil.
  - Modification at the buck converter circuit to regulate VCC to steady 3 V.
  - Voltage dividers for the ADC channels of nDS.
- Firmware
  - Sampling and signal filtering of VCC and VBAT.
  - The algorithm is modified with the new window of 200 mV - 250 mV.

Chapter 5

Receiver Board

Once selected, the optimal RX and coil with all the hardware modifications required. The objective is to develop an RX board to be attached to nDS. The RX board includes the LTC4124 circuit, the buck-converter circuit, the voltage dividers for VCC and VBAT, and the LC tank with the selected coil of 19 mm. The design of the PCB took into consideration several requirements:

- Low current consumption in discharge mode
- Compatibility with nDS
- Flexibility for tests purposes
- Compact layout
- LC tank with minimal interference
- Capability to identify the status of the recharge process

To this end, additional hardware changes were required.

5.1 Switch Circuits

The voltage dividers that allow the nDS ADC to function properly have the disadvantage of consuming additional current even in discharge mode. For this reason, it was necessary to add switches to both VCC and VBAT voltage divider circuits allowing the interrupting of the current in discharge mode (Fig. 5.1). The TPS22916 switch was taken into consideration. The TPS22916 is a small load switch that operates on a single channel and employs a P-Channel MOSFET with low leakage characteristics, ensuring minimal power loss [41]. The TPS22916 has been considered an optimal switch for this application for the following reasons:

- Input voltage range of 1 V to 5.5 V compatible with VCC and VBAT ranges
- Output voltage range of 0V to 5.5 V compatible with VCC and VBAT ranges
- V_{IH} from 1 V to 5.5 V compatible with the V_{0H} of nDS pin of 3 V [35]
- V_{IL} from 0 V to 0.35 V compatible with the V_{0L} of nDS pin of 0 V [35]
- ON-resistance (RON) is around 120 mΩ, which is sufficiently small compared to the resistances of the voltage dividers (39 kΩ and 56 kΩ)
- Current consumption of only 0.5 µA at ON state and 10 nA at OFF state
- Maximum continuous current of 2 A
- Switching time of microseconds order, which is sufficiently low since the first sample is taken after 1 millisecond after the activation switch
- Sufficient small sizes (0.74 mm X 0.74 mm)

According to the datasheet, it is recommended to use an input capacitor with a sufficiently high capacitance (typically 1 µF) to ensure voltage stability. In this case, a capacitor of 10 µF was chosen for a more reliable input voltage. Regarding the output capacitor, the datasheet explains that a lower capacitance value results in a faster falling time when the switch is disabled. Therefore, a capacitor of 0.1 µF was selected for the output capacitor.

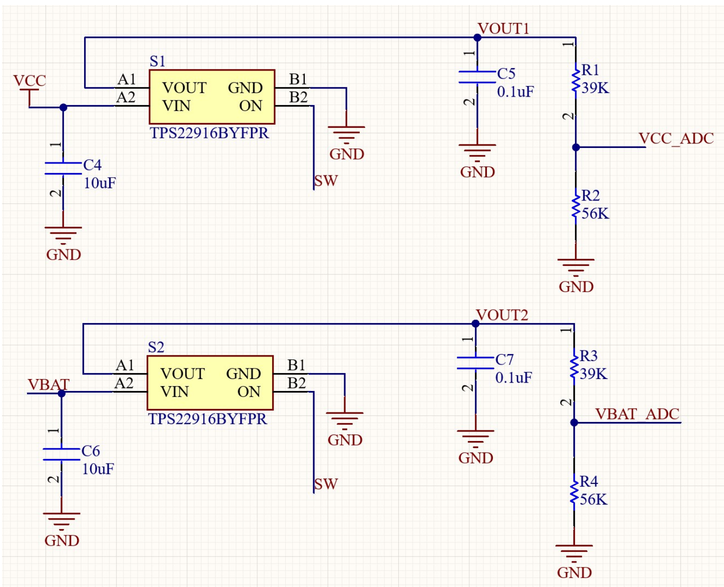

Figure 5.1: Voltage dividers with switches for ADC channels.

5.2 Recharge Status Circuit

During the recharge process, the LTC4124 provides a feature to monitor the recharge status by using a led connected to the CHRG pin [30]. In an implantable device, the led wouldn't be useful; therefore, a different technique needs to be implemented to monitor the recharge status process. After all modifications, only one pin of nDS remained available, which is needed to monitor the CHRG pin. Hence, no active components or switches can be added to the design. An optimal solution is to develop a voltage divider, as shown in figure 5.2, where nDS can read the square voltage across R_{LED1}, computes the frequency, and determines in which status is the recharge based on table 2.1. The datasheet provides information only for V_{nDS} at 1.8 V and 3.8 V [35]. Therefore, the design considered the conditions at 3.8 V, which were the most restrictive. The requirements for the selection of the value of R_{LED1} and R_{LED2} are the following:

- During the recharge phase, the high level of V_{CHRG} (V_{CHRGOH}) must be below 3 V, the maximum admissible voltage for the pins of nDS, and above 1.67 V, which is V_{TH} with no hysteresis for V_{nDS} at 3.8 V.

- During the recharge phase, the low level of V_{CHRG} (V_{CHRGOL}) just need to be below V_{TH} with no hysteresis.

- During the discharge phase, the current consumption I_{LED} of the status circuit must be below 50 µA to ensure low power consumption.

- During the recharge phase, when V_{CHRG} is high, the circuit must provide enough current to make the pin sense a high voltage level.

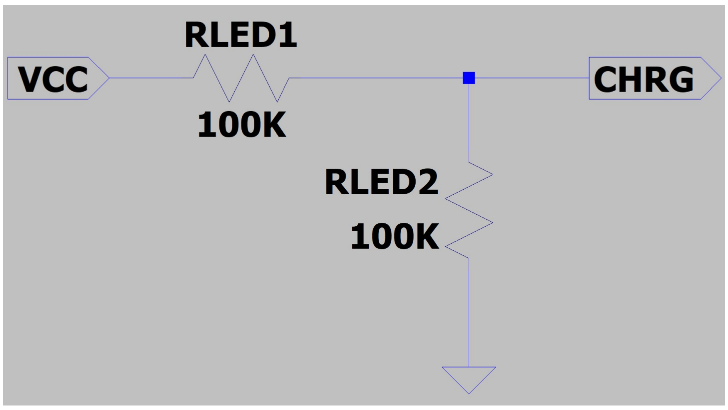

Figure 5.2: Recharge Status Circuit.

During the recharge phase, using the voltage divider, when the CHRG is at V_{CHRGOH}, the open-drain current source of maximum 300 µA is disabled. Consequently, no current flows into R_{LED1}, and the V_{CHRGOH} is equal to VCC. While when the CHRG is at V_{CHRGOL}, the current is flowing in R_{LED1}, and thus V_{CHRGOL} is equal to $VCC - I_{RLED1} \cdot R_{LED1}$. R_{LED1} and R_{LED2} were chosen to be both at 100 kΩ, to satisfy the requirements. Figure 5.3 shows in yellow the V_{CHRG} and in purple VCC pin with the LTC4124 custom board modified adding R_{LED1} and R_{LED2}. The CHRG pin at V_{CHRGOH} is $\frac{VCC}{2}$, making the V_{CHRGOH} spanning from 1.7 V to 2.5 V, while at V_{CHRGOL} is a 0 V. During the discharge phase, I_{LED} would be ranging from 17 µA to 20.5 µA depending on VCC.

Figure 5.3: V_{CHRG} and VCC during normal recharging process (CHRG on CH1 and VCC on CH3).

A test was performed to ensure that the circuit could provide sufficient current to the pin of nDS allowing it to recognize correctly V_{CHRGOH} and V_{CHRGOL}. The LTC4124 custom board was modified, adding R_{LED1} and R_{LED2}, and software modifications were implemented only for test purposes. PTH was fixed at 250 mV, and the DIOI4 pin of nDS checked for variations in input every 10 milliseconds. If a variation is detected, the DIOI5 pin outputs the high or low level accordingly. Figure 5.4, shows in yellow V_{CHRG} and in purple DIOI5 pin output. The results obtained prove the reliability of the developed Recharge Status Circuit

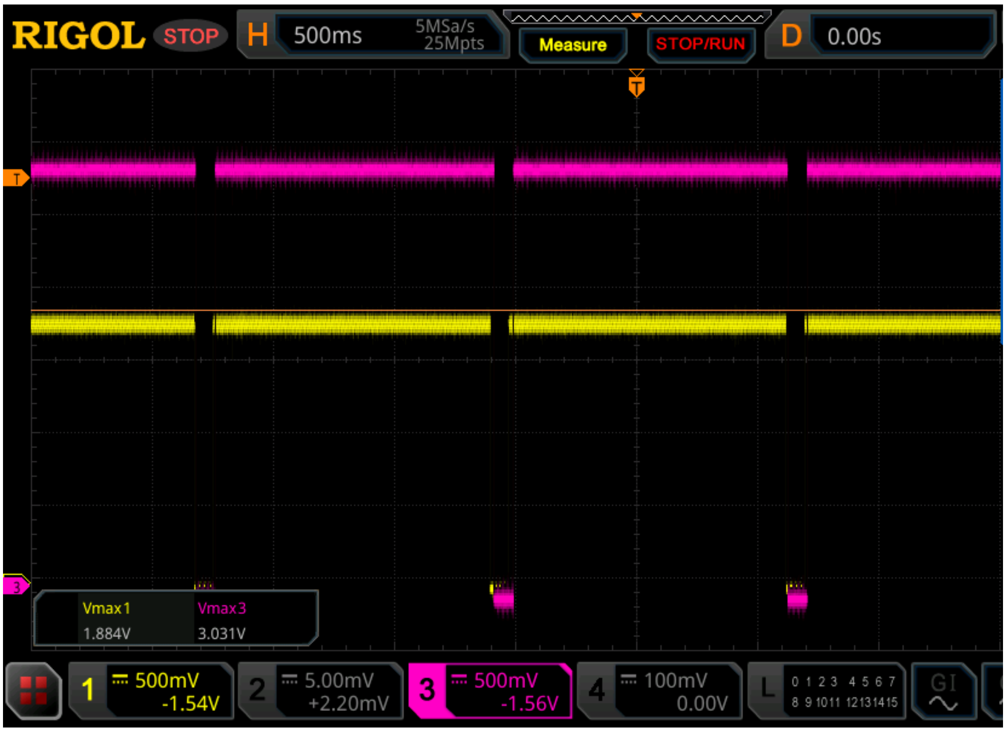

Figure 5.4: Test Recharge Status Circuit (CHRG on CH1 and DIOI5 on CH3).

During the discharge phase, it was measured with the DMM7510 7.5 Digit Graphical Sampling Multimeter that nDS had an average current consumption of 49 µA. A resistor of 470 kΩ was placed to simulate the load of nDS, and a test during the discharge phase was performed using the LIR2025 battery at 3.8 V to measure the current consumption of the battery (I_{BAT}). It was measured with the RS-660 multimeter that before the implementation of the Recharge Status Circuit I_{BAT} was 36 µA, after the implementation I_{BAT} increased, as expected, at 56 µA.

5.3 Board Design

Figure 5.5 shows the electrical schematic of the receiver board, which can be divided into four main blocks: the LTC4124 circuit, the buck-converter circuit, the voltage dividers for VCC and VBAT, and the LC tank. In the LTC4124 circuit, the DCIN and NTC pin were interconnected using custom-designed bridge solders. This arrangement allows for enabling or disabling these features if needed for test purposes. During the discharge mode, it was observed that enabling the DCIN pin results in an additional current consumption of approximately 300 µA. Despite this increase in power consumption, the option to use the DCIN pin was retained because it facilitates a swift transition to the discharge mode, which is useful for further testing. When the battery is connected, applying an impulse to the DCIN pin causes the VCC voltage to closely approach the VBAT voltage, thus entering discharge mode. Similarly, even if enabling the NTC pin would cause an additional current consumption of typically 28 µA [30], it is useful to monitor the battery's temperature. Regarding the LC tank, two capacitors were used, but only CRx2 (22 µF) was needed to achieve the resonance frequency of 200 KHz with the 19 mm coil. The CRx1 footprints were included to ensure flexibility if the coil needs to be changed in future works. The buck-converter circuit and the voltage dividers are designed as described previously.

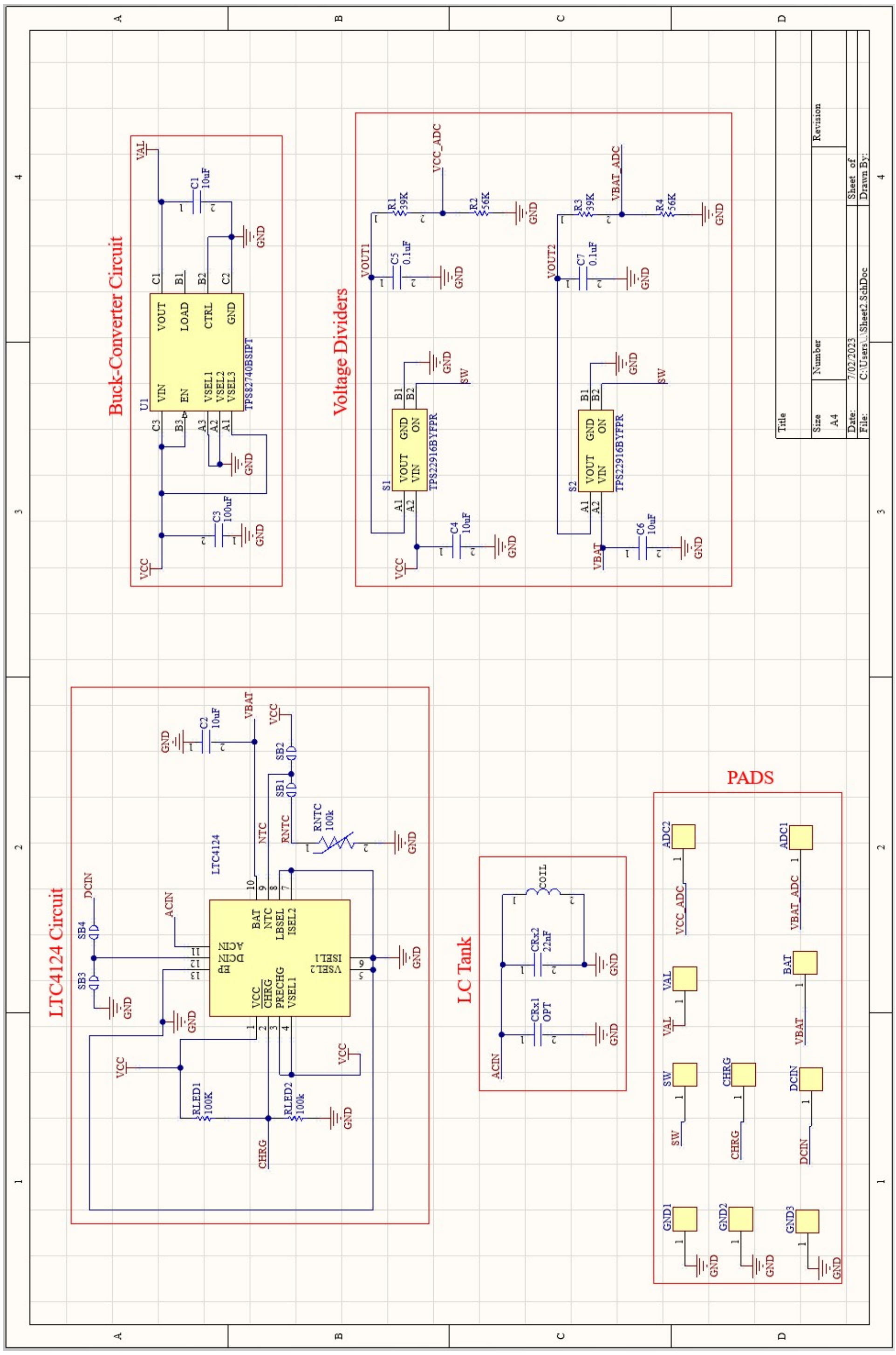

Figure 5.5: Receiver Board Schematic.

Figure 5.6 illustrates the layout of the receiver board, which has dimensions of 12 mm x 14 mm. The outlines of the board were deliberately designed to match those of nDS, allowing for convenient placement of the receiver board either beside or on top of the nDS board. Figure 5.7 shows the device's two possible board configurations. Two polygon pours were implemented on the top and bottom layers of the board to enhance the VCC and GND connections. The top layer was dedicated to VCC, while the bottom layer was used for the GND. To create equal distances between components and ensure a balanced layout, the LTC4124 was placed in the middle of the board. The LC tank was placed as close as possible to the ACIN pin, and the traces used to make the connection were thicker than the others, ensuring a short and direct connection to minimize any potential interference. At the sides of the LTC4124, the voltage divider circuits for VCC and VBAT are placed, facilitating the signal routing. Each circuit includes the necessary components, such as the input capacitor, the switch, the output capacitor, and the resistors for partitioning, arranged as suggested by the TPS22916 datasheet [41]. The buck converter circuit, implemented to convert the VCC voltage to 3 V, was placed beneath the LTC4124 to make the PCB more compact. The components of the buck converter circuit were arranged in a specific order: firstly, the input capacitor was placed to handle the incoming voltage, then the TPS82740B, which serves as the DC/DC converter, and finally, the output capacitor to stabilize the converted 3 V output. The resistors R_{LED1} and R_{LED2} of the Recharge Status Circuit were placed close to the CHRG pin, ensuring maximum compactness and minimal signal interference. All the components, except the RNTC footprints, were located on the top layer of the board. While on the bottom layer, the designed pads were placed to connect the necessary signals to the nDS, including pads for attaching the battery and pads for connecting the coil. The RNTC must be placed on the bottom layer to be in contact with the battery.

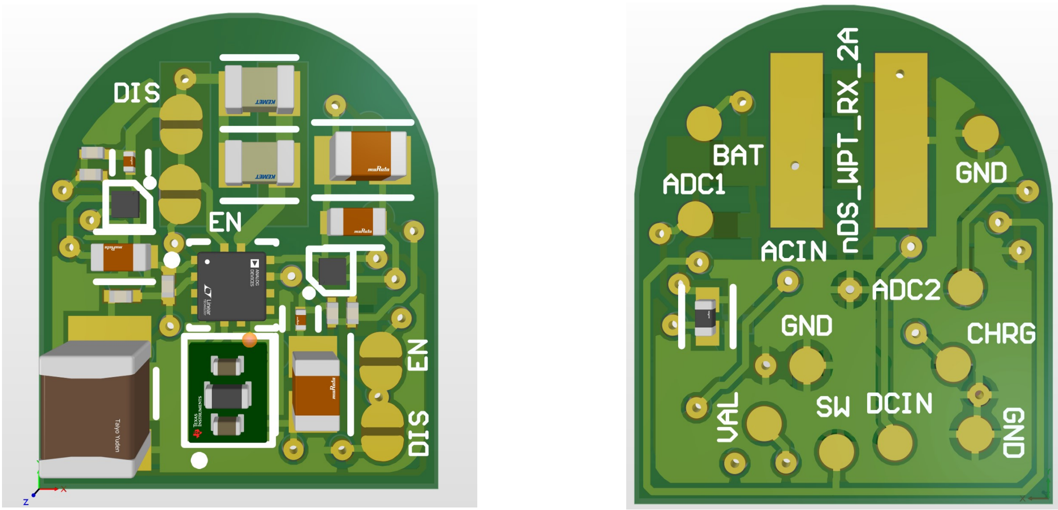

(a) (a)

Figure 5.6: Receiver board schematic: a) Top view; b) Bottom view.

(a) (b)

Figure 5.7: Boards configurations: a) Stacked configuration; b) Lateral configuration.

Chapter 6

Conclusion and Future Perspectives

The main features and functionalities of nDS have been discussed. WPT systems using different methods have been compared, resulting in the NRIC technique as the best technique to implement in AIMDS, because it has a power output suitable for AIMDs, uses low operating frequencies, and has a power transmission range similar to the skin's thickness. The requirements needed for the implementation of WPT for nDS are: optimal receiver in terms of efficiency, optimal coil in terms of efficiency and size, reliability of recharge process, high power transmission efficiency, low heat dissipation, and low sensitivity to any misalignment of the RX coil. A WPT system developed in previous works and TX and RX used have been studied to achieve these goals. However, hardware and software modifications were required to create a suitable device for in vivo-test. The hardware modifications to the WPT systems employed were: the PTH circuit's modification through the additional control on PTHM allowing to transmit more power, the design of the buck-converter circuit to power nDS, the design of the voltage dividers for the ADC of nDS and the implementation of a temperature RX monitor circuit for testing purposes. The firmware modifications involved the ADC of nDS and the change of the window size of the algorithm. Customized boards were developed to find the optimal RX between the LTC4124 and the LTC4126, which appeared to be the LTC4124. Characterizations of different RX coils were made alongside recharge tests, where the best coil in terms of size, efficiency, robustness, and low heat dissipation resulted in being the 19 mm coil with a peak efficiency of 32.3% at 6.5 mm of distance between TX and RX coils and with a temperature increase of only 1.7 °C. It was proved that the temperature increase is further reduced in an in-vivo test. It was also demonstrated that a 200 mV - 250 mV window was more efficient than a 300 mV - 700 mV window. A compatible RX board was designed to be attached to nDS. The board design requirements were low current consumption in discharge mode, capability to identify the recharge status, flexibility for tests purposes, compact layout, minimal interference of the LC tank, and compatibility with nDS. Switches were introduced at the voltage dividers of VCC and VBAT to ensure low current consumption. The Recharge Status Circuit was introduced to identify the recharge status process. The design of the RX board was studied to ensure flexibility by introducing customized solder bridges. Suitable placement of the components assured the compactness of the layout. Minimal interference of the LC tank was achieved by an optimal arrangement with increasing the width of the traces used for the tank connections. Moreover, compatibility with nDS was reached by placing the necessary pads and employing a compatible layout for the RX board. However, several improvements can still be performed. On the hardware side, the feedback circuit of the LTC4125 can be completely deleted by connecting the FB pin directly to GND, since the close-loop control is employed and the PTH circuit of the TX can be completely substituted with the control signal at PTHM, since PTHM controls PTH. On the firmware side, a code for controlling the switches of VCC and VBAT voltage dividers needs to be implemented. The code should enable the switches before the ADC sampling and disable them after it. In addition, a code for controlling the Recharge Status Circuit needs to be implemented. The code should read the square wave's pulse width at the CHRG pin and select which status is the recharge process using the computed frequency. Moreover, several tests should be conducted including: tests on the RX board developed with nDS to find the optimal configurations with nDS, in-vivo tests to verify that the power transmission is stable with minimal low heat dissipation, and tests, in discharge mode, to evaluate the duration of the battery.

Appendix A

Appendix A

This appendix presents the software modifications of Del Bono's code in order to allow the Sensor Controller CPU to handle the sampling of the ADC channels. The main modifications regard the handling of the interrupt generated by the Sensor Controller CPU, the addition median filtering, and the conversion of the values.

This is the task performed by the Sensor Controller CPU, which samples the ADC channels every millisecond.

```
timer1Start(TIMER1_MODE_PERIODICAL, 94, 8);// Generate timer event
    after 1 ms
// Enable the ADC (fixed reference,2.7 us sample time,  trigger
    Manual)
adcEnableSync(ADC_REF_VDDS_REL,ADC_SAMPLE_TIME_2P7_US,
    ADC_TRIGGER_MANUAL);
for (U16 n = 0; n < num_campioni; n++) {
    // Wait for timer event before read adc
    timer1Wait();
    // Select ADC input Vbat
    adcSelectGpioInput(AUXIO_A_VBAT_PIN);
    //gen manual trigger for adc
    adcGenManualTrigger();
    //read adc and place value in buffer for Vbat
    adcReadFifo(output.Vbatvett[n]);
    // Select ADC input Vcc
    adcSelectGpioInput(AUXIO_A_VCC_PIN);
    //gen manual trigger for adc
    adcGenManualTrigger();
    //read adc and place value in buffer for Vcc
    adcReadFifo(output.Vccvett[n]); }
timer1Stop(); //stop timer
adcDisable(); //diseable adc
fwGenAlertInterrupt();// gen allert for application
```

In these lines of code the Sensor Controller CPU transfers the measured data to the main CPU.

```
// SCIF driver callback: Sensor Controller task code has generated an
    alert interrupt
void scTaskAlertCallback(void) {
    // Clear the ALERT interrupt source
    scifClearAlertIntSource();
//    ... Access Sensor Controller task data structures here ...

//fill vector vbat
    for (int n = 0; n < SCIF_MODIFICA_ADC_NUM_CAMPIONI; n++) {
        vbat[n] = scifTaskData.modificaAdc.output.Vbatvett[n];
    }

//fill vector vcc
    for (int n = 0; n < SCIF_MODIFICA_ADC_NUM_CAMPIONI; n++) {
        vcc[n] = scifTaskData.modificaAdc.output.Vccvett[n];
    }
    // Acknowledge the ALERT event
    scifAckAlertEvents();
}
```

In these lines of code the CPU performs the median filtering and the conversions of the values

```
static void SimplePeripheral_performPeriodicTask(void)
{
    //Start task only if Sensor Controller has been enabled
    if(scif_flag==1){

        //wait task to be finished
        while(scifWaitOnNbl(0) != SCIF_SUCCESS);

        scifResetTaskStructs(BV(SCIF_MODIFICA_ADC_TASK_ID),BV(
    SCIF_STRUCT_OUTPUT)); //reset data struct_output task

        scifExecuteTasksOnceNbl(BV(SCIF_MODIFICA_ADC_TASK_ID));
    //exceute task

        //compute Median

        for (int pass=0; pass<NUM_CAMPIONI-1; pass++){
            for (int i=0; i<NUM_CAMPIONI-pass-1; i++){
              if(vcc[i]>vcc[i+1]){
              hold=vcc[i+1];
              vcc[i+1]=vcc[i];
              vcc[i]=hold;
              }
              if(vbat[i]>vbat[i+1]){
              hold1=vbat[i+1];
              vbat[i+1]=vbat[i];
              vbat[i]=hold1;
              }
           }
        }
       // if NUM_campioni !% 2 (if samples odd) -->vcc_m=(vcc[(
    NUM_CAMPIONI-1)/2])+ vcc[(NUM_CAMPIONI+1)/2])>> 1;

           vcc_m =(vcc[(NUM_CAMPIONI)/2])*1.284;//(3000/4096)*(95/56)
           vbat_m =(vbat[(NUM_CAMPIONI)/2])*1.284;
    }
```

Bibliography

[1] Derrick Wing Kwan Ng, Trung Q Duong, Caijun Zhong, and Robert Schober. «The Era of Wireless Information and Power Transfer». eng. In: *Wireless Information and Power Transfer*. 1st ed. Wiley - IEEE. United Kingdom: Wiley, 2018, pp. 1–16. ISBN: 9781119476795 (cit. on p. 1).

[2] Sadeque Reza Khan, S.K. Pavuluri, Gerard Cummins, and M.P.Y. Desmulliez. «Wireless Power Transfer Techniques for Implantable Medical Devices: A Review». In: *Sensors* 20 (June 2020), p. 3487. DOI: 10.3390/s20123487 (cit. on pp. 1, 5, 6).

[3] Junho Kim, Hyeok Kim, Dongwook Kim, Hun-Jun Park, Kiwon Ban, Seungyoung Ahn, and Sung-Min Park. «A Wireless Power Transfer Based Implantable ECG Monitoring Device». In: *Energies* 13.4 (2020). ISSN: 1996-1073. DOI: 10.3390/en13040905. URL: https://www.mdpi.com/1996-1073/13/4/905 (cit. on pp. 1, 5).

[4] Mitchell Kline, Igor Izyumin, Bernhard Boser, and Seth Sanders. «Capacitive power transfer for contactless charging». In: (Apr. 2011), pp. 1398–1404. DOI: 10.1109/APEC.2011.5744775 (cit. on pp. 1, 5).

[5] Shaul Ozeri and Doron Shmilovitz. «Ultrasonic transcutaneous energy transfer for powering implanted devices». In: *Ultrasonics* 50 (May 2010), pp. 556–66. DOI: 10.1016/j.ultras.2009.11.004 (cit. on pp. 1, 5).

[6] Nicola Di Trani et al. «Remotely controlled nanofluidic implantable platform for tunable drug delivery». In: *Lab on a Chip* 19 (13 July 2019), pp. 2192–2204. ISSN: 14730189. DOI: 10.1039/c9lc00394k (cit. on pp. 1, 3, 4).

[7] L Davidson. «Human genetic databases on the Internet: a webliography». en. In: *Med. Ref. Serv. Q.* 16.2 (1997), pp. 49–54 (cit. on p. 3).

[8] Shan-Yang Lin and Yoshiaki Kawashima. «Current status and approaches to developing press-coated chronodelivery drug systems». In: *Journal of Controlled Release* 157.3 (2012), pp. 331–353. ISSN: 0168-3659. DOI: https://doi.org/10.1016/j.jconrel.2011.09.065. URL: https://www.

sciencedirect.com/science/article/pii/S0168365911008509 (cit. on p. 3).

[9] Gagandeep Kaur, Maya Saba, Craig L. Phillips, Keith Wong, and Bandana Saini. «Education Intervention on Chronotherapy for Final-Year Pharmacy Students». In: *Pharmacy* 3.4 (2015), pp. 269–283. ISSN: 2226-4787. DOI: 10.3390/pharmacy3040269. URL: https://www.mdpi.com/2226-4787/3/4/269 (cit. on p. 3).

[10] Fabiana Del Bono, Andrea Bontempi, Nicola Di Trani, Danilo Demarchi, Alessandro Grattoni, and Paolo Motto Ros. «Wireless Power Transfer Closed-Loop Control for Low-Power Active Implantable Medical Devices». In: vol. 2022-October. Institute of Electrical and Electronics Engineers Inc., 2022. ISBN: 9781665484640. DOI: 10.1109/SENSORS52175.2022.9967268 (cit. on pp. 4, 10, 19, 20, 24, 25, 27, 30, 31, 33, 38, 53, 56).

[11] H. Hertz. «Ueber sehr schnelle electrische schwingungen». In: 267 (May 1887), pp. 421–448 (cit. on p. 5).

[12] Anh M. Le, Linh H. Truong, Toan V. Quyen, Cuong V. Nguyen, and Minh T. Nguyen. «Wireless Power Transfer Near-field Technologies for Unmanned Aerial Vehicles (UAVs): A Review». In: *EAI Endorsed Transactions on Industrial Networks and Intelligent Systems* 7.22 (Jan. 2020). DOI: 10.4108/eai.31-1-2020.162831 (cit. on p. 5).

[13] Luke Hutchinson, Ben Waterson, Bani Anvari, and Denis Naberezhnykh. «Potential of wireless power transfer for dynamic charging of electric vehicles». In: *IET Intelligent Transport Systems* 13.1 (2019), pp. 3–12. DOI: https://doi.org/10.1049/iet-its.2018.5221. eprint: https://ietresearch.onlinelibrary.wiley.com/doi/pdf/10.1049/iet-its.2018.5221. URL: https://ietresearch.onlinelibrary.wiley.com/doi/abs/10.1049/iet-its.2018.5221 (cit. on p. 5).

[14] Naoto Takayama, Shogo Asaka, Taku Shimizu, Shuhei Toga, Koutarou Ozawa, and Sousuke Nakamura. «Research on WPT-Robot: Development of a Simultaneous Tracking and Charging Function». In: (2022), pp. 978–978. DOI: 10.1109/SII52469.2022.9708897 (cit. on p. 5).

[15] Cuong M. Nguyen, Pavan Kumar Kota, Minh Q. Nguyen, Souvik Dubey, Smitha Rao, Jeffrey Mays, and J.-C. Chiao. «Wireless Power Transfer for Autonomous Wearable Neurotransmitter Sensors». In: *Sensors* 15.9 (2015), pp. 24553–24572. ISSN: 1424-8220. DOI: 10.3390/s150924553. URL: https://www.mdpi.com/1424-8220/15/9/24553 (cit. on p. 5).

[16] Manal Adeeb, Ashraf Islam, Mohammad Haider, F. Tulip, Nance Ericson, and S. Islam. «An Inductive Link-Based Wireless Power Transfer System for Biomedical Applications». In: *Active and Passive Electronic Components* 2012 (May 2012). DOI: 10.1155/2012/879294 (cit. on p. 5).

[17] Sai Chun Tang, Tian Le Tim Lun, Ziyan Guo, Ka-Wai Kwok, and Nathan J. McDannold. «Intermediate Range Wireless Power Transfer With Segmented Coil Transmitters for Implantable Heart Pumps». In: *IEEE Transactions on Power Electronics* 32.5 (2017), pp. 3844–3857. DOI: 10.1109/TPEL.2016.2584558 (cit. on p. 5).

[18] Roya Sheybani, Angelica Cobo, and Ellis Meng. «Wireless programmable electrochemical drug delivery micropump with fully integrated electrochemical dosing sensors». In: *Biomedical microdevices* 17 (Aug. 2015), p. 9980. DOI: 10.1007/s10544-015-9980-7 (cit. on p. 5).

[19] Chunyan Xiao, Kangzheng Wei, Dingning Cheng, and Yufeng Liu. «Wireless Charging System Considering Eddy Current in Cardiac Pacemaker Shell: Theoretical Modeling, Experiments, and Safety Simulations». In: *IEEE Transactions on Industrial Electronics* 64.5 (2017), pp. 3978–3988. DOI: 10.1109/TIE.2016.2645142 (cit. on p. 5).

[20] Han Joon Kim, Hiroshi Hirayama, Sanghoek Kim, Ki Jin Han, Rui Zhang, and Ji Woong Choi. «Review of Near-Field Wireless Power and Communication for Biomedical Applications». In: *IEEE Access* 5 (Sept. 2017), pp. 21264–21285. ISSN: 21693536. DOI: 10.1109/ACCESS.2017.2757267 (cit. on p. 5).

[21] Hao Jiang et al. «A Low-Frequency Versatile Wireless Power Transfer Technology for Biomedical Implants». eng. In: *IEEE transactions on biomedical circuits and systems* 7.4 (2013), pp. 526–535. ISSN: 1932-4545 (cit. on p. 5).

[22] Anil Kumar RamRakhyani, Shahriar Mirabbasi, and Mu Chiao. «Design and Optimization of Resonance-Based Efficient Wireless Power Delivery Systems for Biomedical Implants». In: *IEEE Transactions on Biomedical Circuits and Systems* 5.1 (2011), pp. 48–63. DOI: 10.1109/TBCAS.2010.2072782 (cit. on p. 5).

[23] Kush Agarwal, Rangarajan Jegadeesan, Yong-Xin Guo, and Nitish V. Thakor. «Wireless Power Transfer Strategies for Implantable Bioelectronics». eng. In: *IEEE reviews in biomedical engineering* 10 (2017), pp. 136–161. ISSN: 1937-3333 (cit. on pp. 5–8).

[24] Stanley B. Barnett, Hans-Dieter Rott, Gail R. ter Haar, Marvin C. Ziskin, and Kazuo Maeda. «The sensitivity of biological tissue to ultrasound». In: *Ultrasound in Medicine Biology* 23.6 (1997), pp. 805–812. ISSN: 0301-5629. DOI: https://doi.org/10.1016/S0301-5629(97)00027-6. URL: https:

//www.sciencedirect.com/science/article/pii/S0301562997000276 (cit. on p. 6).

[25] R. Jegadeesan and Yong-Xin Guo. «Topology Selection and Efficiency Improvement of Inductive Power Links». eng. In: *IEEE transactions on antennas and propagation* 60.10 (2012), pp. 4846–4854. ISSN: 0018-926X (cit. on p. 8).

[26] Pablo Pérez-Nicoli, Fernando Silveira, and Maysam Ghovanloo. *Inductive Links for Wireless Power Transfer*. Springer International Publishing, 2021. DOI: 10.1007/978-3-030-65477-1 (cit. on pp. 8, 9, 44, 45, 48).

[27] Reem Shadid and Sima Noghanian. «A Literature Survey on Wireless Power Transfer for Biomedical Devices». eng. In: *International journal of antennas and propagation* 2018 (2018), pp. 1–11. ISSN: 1687-5869 (cit. on p. 8).

[28] V. Fuentes and T. Roz. «Using low power transponders and tags for RFID applications». In: *EM Microelectron. Marin SA, Marin* 1998 () (cit. on p. 9).

[29] Supervisors Danilo Demarchi Paolo Motto Ros Antonia Silvestri Candidate Andrea Bontempi. *Wireless power transfer for implantable medical devices*. 2021 (cit. on pp. 10, 19, 24–27, 30, 31, 45, 54, 56).

[30] *LTC4124 100 mA Li-Ion Charger with Low Battery Disconnect*. Rev. A. Analog Devices. 2019. URL: https://www.analog.com/en/products/ltc4124.html (cit. on pp. 10–12, 14, 33, 41, 56, 62, 65).

[31] *LTC4126 7.5 mA Wireless Li-Ion Charger with 1.2 V Step-Down DC/DC Converter*. Rev. A. Analog Devices. 2019. URL: https://www.analog.com/media/en/technical-documentation/data-sheets/ltc4126.pdf (cit. on pp. 15, 17, 18, 41).

[32] *LTC4124/LTC4125, 500 mA Wireless Li-Ion Charger Demonstration Kit*. Rev. A. Analog Devices. 2021. URL: https://www.analog.com/media/en/%20dsp-documentation/evaluation-kit-manuals/DC2770A-B-KIT.pdf (cit. on pp. 19, 27, 29, 40).

[33] *LTC4125 5 W AutoResonant Wireless Power Transmitter*. Analog Devices. 2015. URL: https://www.analog.com/en/products/ltc4125.html (cit. on pp. 21–26, 28, 29, 32, 45, 56).

[34] *DEMO MANUAL DC2663A-KIT*. Analog Devices. 2019. URL: https://www.analog.com/media/en/technical-documentation/user-guides/DC2663A-KIT.pdf (cit. on pp. 31, 40).

[35] *CC2640R2F SimpleLink™ Bluetooth® low energy Wireless MCU datasheet*. Rev. C. Texas Instruments. 2020. URL: https://www.ti.com/lit/ds/symlink/cc2640r2f.pdf (cit. on pp. 31, 33, 35, 61, 62).

[36] *TPS82740x 360-nA IQ MicroSIP Step Down Converter Module for Low Power Applications*. Texas Instruments. 2014. URL: `https://www.ti.com/lit/ds/symlink/tps82740b.pdf` (cit. on p. 33).

[37] *TPS82740xSIPEVM-617 User's Guide*. Texas Instruments. 2014. URL: `https://www.ti.com/lit/ug/slvua72/slvua72.pdf` (cit. on p. 34).

[38] *BS EN 45502-1:1998: Active implantable medical devices: General requirements for safety, marking and information to be provided by the manufacturer*. 1998 (cit. on pp. 34, 59).

[39] Tasneem Poonawalla and Dayna Diven. *Anatomy of the Skin*. 2008. URL: `https://www.utmb.edu/pedi_ed/CoreV2/Dermatology/page_03.htm` (cit. on pp. 44, 53).

[40] K. Hynynen, D. Deyoung, M. Kundrat, and E. Moros. «The effect of blood perfusion rate on the temperature distributions induced by multiple, scanned and focused ultrasonic beams in dogs' kidneys in vivo». In: *International Journal of Hyperthermia* 5.4 (1989). PMID: 2746052, pp. 485–497. DOI: `10.3109/02656738909140473`. URL: `https://doi.org/10.3109/02656738909140473` (cit. on p. 54).

[41] *TPS22916xx 1-V–5.5-V, 2-A, 60-m Ultra-Low Leakage Load Switch*. Rev. F. Texas Instruments. 20197. URL: `https://www.ti.com/lit/ds/symlink/tps22916.pdf` (cit. on pp. 60, 67).